EPITHERMAL NEUTRON ACTIVATION ANALYSIS OF SHORT-LIVED RADIONUCLIDES USING A PNEUMATIC TRANSPORT SYSTEM AND A PULSED D-T NEUTRON GENERATOR

BY
RICHARD J. KUSTRA

THESIS

Submitted in partial fulfillment of the requirements
for the degree of Master of Science in Nuclear, Plasma, and Radiological Engineering
in the Graduate College of the
University of Illinois at Urbana-Champaign, 2016

Urbana, Illinois

Master's Committee:
Professor Brent J. Heuser, Advisor
Associate Professor Ling-Jian Meng

ABSTRACT

A pneumatic transport system for the detection and characterization of short-lived (of order 60 s or less) radionuclides produced during irradiation by a D-T neutron generator was constructed. Target samples of indium, palladium, and germanium were irradiated by the neutron generator embedded in a graphite monolith to produce epithermal activation products. The three radioisotopes of interest are palladium-107, palladium-109, and germanium-75. The experimental half-lives of each of the three isotopes, with the specific activity in parenthesis are: 21.82 ± 3.71 (49.36 nCi/g), 279.21 ± 27.80 (158.91 nCi/g), and 48.51 ± 12.58 (504.78 nCi/g) respectively. These experimental half-lives agree with the published half-lives.

The Monte Carlo N-Particle (MCNP) radiation transport code was used to model the graphite pile, the pneumatic transport tube, and the neutron generator. This resulted in benchmarking and validation of the experimental results. In order to reach an agreement between the experimental results and MCNP, a modification was required to the neutron absorption reaction rate produced from MCNP using isomeric to ground state ratios to accurately account for the decay mode most common with these short-lived radioisotopes.

ACKNOWLEDGMENTS

I would like to acknowledge and thank the following people and organizations. My advisor, Prof. Brent Heuser, for his great insight, guidance, support and assistance in the completion of this thesis work. I would also like to thank Prof. Ling-Jian Meng for his additional comments on my thesis. I would also like to thank my girlfriend, Jessica Bush, and my parents for supporting me throughout my master's degree. Dr. Stoyan Toshkov for assisting me in acquiring the necessary materials on time and his support. And finally, all those who have been involved during the research are gratefully acknowledged for their help.

This project was supported by the UIUC COE SRI Program and US NRC Grant No. NRC-HQ-12-G-38-0080.

Table of Contents

List of Figures

List of Tables

CHAPTER 1: INTRODUCTION AND LITERATURE REVIEW

Neutron activation analysis enables scientists to perform elemental/isotopic measurements with high-sensitivity, reliability, and reproducibility with simple sample preparation [1]. Between the mid-1950s to the present day, the use of neutron activation analysis increased due to the reasons listed above over identification of elements using chemical reactions. Neutron activation analysis shows that, fundamentally, all that is required are a source of neutrons with a known flux or standard reference material, a target to bombard with neutrons, a detailed description of target neutron absorption cross section, and a method of detecting particles from the resulting interaction [1]. This method can be coupled to a pneumatic transport system to study short-lived radioisotopes with a neutron generator as the neutron source, as is presented here.

The pneumatic transport system coupled to a low-flux neutron generator will show it is possible to activate various target materials, with varying neutron capture cross sections, and detect short-lived radioisotopes without the requirement for a reactor or high-flux environment. The energy of the neutrons emitted from the D-T neutron generator is 14.1 MeV. Whereas, the neutron spectrum from a typical light water reactor is thermalized to approximately 0.1 eV, which does not allow for the study of activation products produced by fast neutrons.

1.1 INTRODUCTION TO UIUC SYSTEM AND ISOTOPES

This thesis research addresses the challenges of activating various target materials including isotopes of palladium and germanium using cyclic activation analysis in a non-reactor environment for the explicit purpose of detecting and characterizing short-lived neutron-induced radioisotopes. Figure 1 shows the completed pneumatic transport system with the graphite monolith in the background and the remote counting station in the foreground.

Pneumatic transport systems in nuclear reactors date to that of neutron activation analysis. The use of low flux, high energy neutron generators with pneumatic transport systems is more recent. This is due to innovations in the industry to create compact neutron generators, with the only

drawback of a reduction in source strength.

The purpose of pneumatic transport systems is to protect semiconductor detectors from radiation damage, reduce the background created by the neutron source by transporting the activated material to a remote detector, and allow for the measurement of radioisotopes produced by neutron activation. Additionally, pneumatic transport systems are essential for the study of short lived activation products with a remote detector station because of the capability of rapidly moving an irradiated sample.

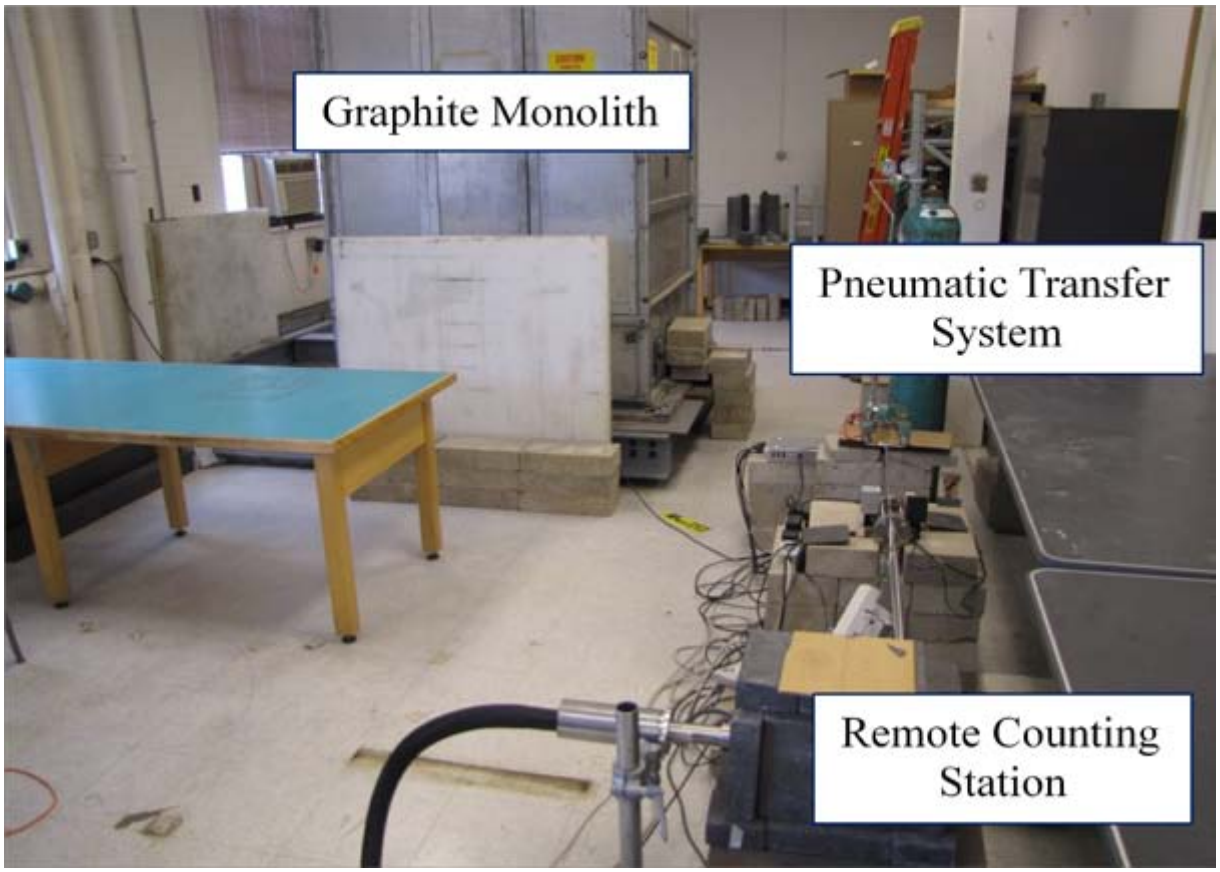

Figure 1: Pneumatic Transport System Construction for this Research

The distinction between this experimental assembly and past systems is the use of a low-flux D-T neutron generator. This fact alone introduces certain challenges that make the work presented in this thesis significant since the neutron flux is orders of magnitude lower than those present within the archived literature presented later.

Neutron activation analysis of short-lived radioisotopes using pneumatic transport systems in reactor environments has been proven to be an effective method in characterizing material composition. The objective of this thesis research is to use a low strength, portable neutron generator to detect and accurately characterize these short-lived radioisotopes in a similar fashion to reactor environments. This also includes the implementation of an accurate model using the Monte Carlo N-Particle (MCNP) radiation transport code to determine the viability of the design and benchmarking the experimental results of the completed system.

The design and construction of the pneumatic transport system will focus on producing a sample transport time that is much shorter than the half lives of the isotopes, used here palladium-105, palladium-107 and germanium-75. Additionally, validation of the operation and measuring the reliability of the system is required. Table 1 shows the half-lives, gamma ray signatures, and intensities of the isotopes that will be irradiated with the neutron generator and transported by the pneumatic transport system. Germanium-75 and palladium-107 are the short-lived radioisotopes of interest; however, indium-116 and palladium-109 are necessary to test the reliability of the pneumatic transport system in the initial testing phase.

Table 1: Published Half Lives and Gamma-Ray Signatures of Various Neutron Activation Products [2]

Isotope	**Half-Life** (s)	**Gamma-Ray Energy** (keV)	**Intensity** (%)
Palladium-107	21.3	214.9	68.7
Palladium-109	279.36	188.9	56
Germanium-75	47.7	139.68	39.36
Indium-116	3257.4	1293.4	84.8

1.2 WORK BY OTHERS

This work focuses solely on gamma emission from the activated target material and does not take into account any other radiative emissions (alpha, beta, neutron). This is because the gamma signature of the radioactive daughter products and their respective half-lives can uniquely identify

the radioisotopes without taking any other radiation emission into account.

Kreiner constructed a pneumatic transfer system for a research reactor environment. After completing construction and initial operation, additional suggestions were offered [3]. The requirements that Kreiner determined to be significant are as follows: the system must have short transport times (much less than the half-life of the nuclide of interest); reproducible measurements; the sample vial must maintain mechanical integrity; a precise measurement of the time in which the sample leaves the neutron source and arrives at the detector is required; and fully automated control of the system is required. After experimentation, Kreiner noted one important point unrelated to the transport system, but to the sample vials construction. Frequent contamination of the gamma-lines existed, due to issues with sample vial integrity, in Kreiner's transport system and ultimately caused unreliable measurements of the peak areas. This unreliability can lead to inconsistencies in the half-life measurements of short-lived activation products especially for quantities of activation product on the order of 10^{-9} Ci.

Paas and Sullivan constructed a pneumatic transport system for the explicit purpose of producing and detecting short-lived nuclides, specifically isotopes of hafnium [4]. Using the schematics given in their published thesis, similar sizing of the transport tube and gas inlet/vent tubing can be applied here because the smaller diameter tubing could achieve quick transport times with relatively low pressure input. They proved a system could achieve transport times of approximately one tenth of a second. Paas and Sullivan demonstrated the feasibility of producing a system in terms of transport times given the schematics presented. This will serve as the baseline for the system to be constructed at the University of Illinois Urbana-Champaign.

Similar to previous work, Ismail *et al*. created a pneumatic transfer system to be used in either a reactor environment or with a neutron generator to detect nuclides from neutron activation with half-lives shorter than one minute [5]. Specific to pneumatic transfer systems described here were the use of high density polyethylene sample vials with internally threaded caps to avoid the

necessity of welding the vials shut before use.

Ismail*et al*. chose to construct the entire system out of plastic and aluminum to avoid long lived activation products due to the relatively short half-life of aluminum-28. To control the pneumatic transfer system, Ismail et al. chose a programmable logic controller over a conventional computer for stability and reliability. Work before Ismail et al. typically used conventional computers to control their systems [3] [4].

Salma and Zemplen-Papp suggest a specific transport time related to the half-life of the activation product of interest and to maximize the detector response for a neutron generator system [6]. The source strength of the neutron generator in their experiment was 3×10^8 neutrons/cm^2/s. In this case the total experimental time was chosen to be $8 \times T_{1/2} + 3$ s. For their pneumatic transport system to produce reproducible results, they determined the sample vial had to weigh between 1 to 4g and the transport time have a variability less than 160 ms.

Due to the relatively large neutron flux present near their neutron source, for an activation product of 26.8 s, their activation time and measurement time was a total of 35 s. Salma and Zemplen-Papp chose a one-shot method over cyclic irradiation due to the strength of their neutron source; however, their total experimental time could be repurposed as a cycling time in a lower flux environment.

Only the method of one-shot irradiation has been discussed so far. However, due to the very low neutron fluxes, approximately 10^4 neutrons/cm^2/s according to simulations performed for the graphite pile with the neutron generator and preliminary experiments presented in the results below, reliance on another experimental procedure must be employed. The other experimental method is referred to as "cyclic activation" [7]. The definition of cyclic activation is a method in which a sample is irradiated for a short period of time relative to the half life, the resulting decay is then measured for a short period of time, and the process is repeated to achieve a cumulative detector response as if detection was continuous. Using cyclic activation is one method to increase

the response of the radionuclide of interest as there is an expectation of small quantities of activation being produced in the target material. Using cyclic activation can ultimately lead to the determination of the half life focusing specifically on short-lived nuclides. These conclusions are very similar to the results that Kreiner applied to the one-shot irradiation method, but are more applicable to low strength neutron sources.

Figure 2 shows the detector response as a function of the experiment time *m*; where m is defined as the number of cycles multiplied by the total counting time per cycle (irradiation and detection) divided by the half life of the isotope of interest [7]. The definition of "conventional" in Figure 2 is the irradiation and detection of the sample only once or what is considered by the literature to be one-shot irradiation. Spyrou shows that cyclic activation yields higher detector response for long counting times, leading to a much higher signal to noise ratio [7].

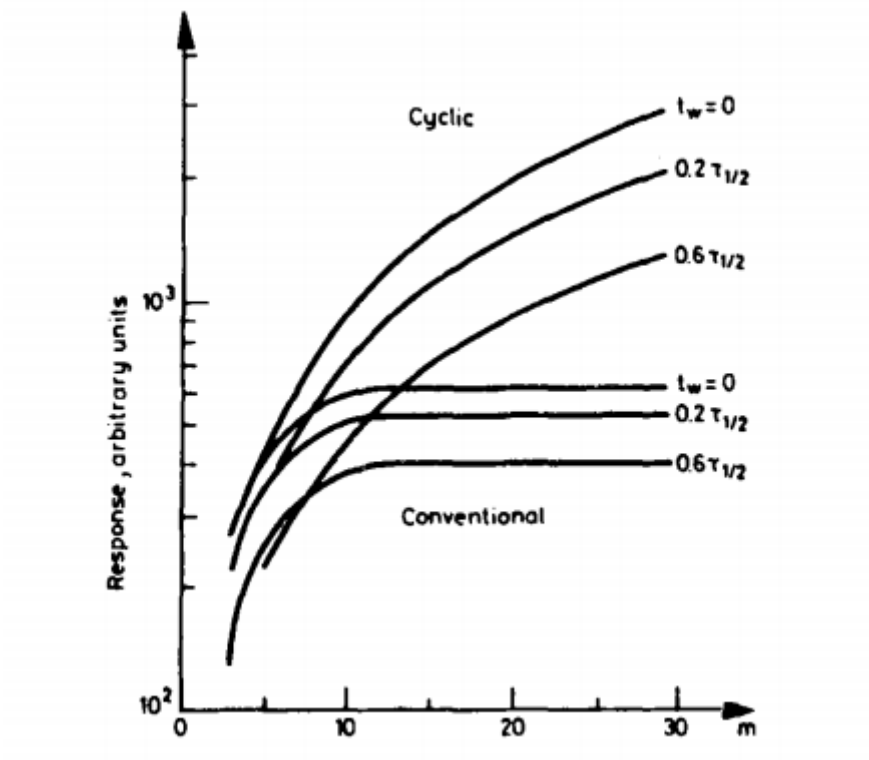

Figure 2: Detector Response between Conventional and Cyclic Counting Methods [7]

It is also suggested that it is not the detector response that should be maximized, but the signal

to noise ratio. The cycling period of the system is ultimately of interest to maximize the detector response. Provided that the pneumatic transport system can move the sample from the neutron source to the detector in at least half of the half-life of the isotope of interest, the system cycling time (t_w) should be between one and five half-lives of a given isotope.

A valid theoretical method to analyze the data is required. Sterlinski discusses the limit of identifying short-lived radioisotopes by gamma-spectroscopy by their half-lives and as a result of experimentation, this analysis resulted in five important conclusions [8], four of which are relevant to this work. According to Sterlinski, when detecting short-lived radioisotopes of low activity, (1) reliance on the half-life as a sufficient condition to identify the radiation being measured, (2) the measurement time of the sample significantly affects the statistical accuracy of the half-life being measured with the only important factor being the ratio of the background to the incident radiation produced by activation, (3) the amount of experimental points should be approximately ten to fifteen between the transport of the irradiated sample to the detector apparatus and ten half lives of the activation product, and (4) if the accuracy of the half-live measurement is less than twenty percent the bias in the measurement is negligible.

Sterlinski mentions that the maximum-likelihood-method (MLM) is a powerful analysis technique that can be applied within this field of study; however, it is ultimately suggested linear least squares should be used instead, as MLM has difficulty solving problems in which the background should be taken into consideration [8]. Sterlinski outlines which type of analytical method should be applied to these types of problems. Specifically, that a well shielded, low-background environment is necessary where ten to fifteen successive measurements can be made post irradiation and apply the linear least squares algorithm to obtain an unbiased half-life. This is what is done here.

CHAPTER 2: THEORETICAL DEVELOPMENT

To characterize count rates expected from the gamma emission of the activation products expected by the detector assembly, the neutron absorption reaction rates produced by the neutron generator must be developed. Duderstadt and Hamilton express the differential frequency as a function of energy of nuclear-nuclear reactions between a neutron and a target nuclei as,

$$\text{interaction frequency}(E) = \nu(E)\Sigma(E), \tag{1}$$

where ν is the speed of the neutron and Σ is the the macroscopic cross section characterizing the reaction of interest [9]. This can be extended to a reaction rate density by multiplying the neutron density by the interaction frequency,

$$F(x,E)dV = \nu(E)\Sigma(E)N(x,E)dV, \tag{2}$$

which is the expected reaction rate at which reactions are occurring [9]. This result can be simplified using the definition of the neutron flux as $\phi(x,E) = \nu(E)N(x,E)$; thus, the differential reaction rate as a function of energy can be written as,

$$R(x,E) = \Sigma(E)\phi(x,E) \tag{3}$$

Integrating the differential reaction rate with respect to energy, the total reaction rate can be characterized by

$$R(t) = V\int_0^\infty N_{Target}(t)\sigma_a(E)\phi(x,E)\,dE, \tag{4}$$

where N_{Target} is the atomic number density of the target material, $\phi(x,E)$ is the differential neutron

flux as a function of space and energy E, $\sigma_a(E)$ is the microscopic neutron absorption cross section as a function of energy [9].

However, a functional form of the neutron flux $\phi(x,E)$ in the target is required to calculate the reaction rate. The coupled first-order partial differential equations, called the lethargy dependent P_1 equations described in Equation 5, allow for a consistent treatment of the slowing down of neutrons in the graphite assembly from the D-T neutron source,

$$\begin{aligned}\frac{\partial J}{\partial x}+\Sigma(u)\phi(x,u) &= \int_u^0 \Sigma_{s0}(u'\to u)\phi(x,u')\,du' + S_0(x,u),\\ \frac{1}{3}\frac{\partial \phi}{\partial x}+\Sigma(u)J(x,u) &= \int_u^0 \Sigma_{s1}(u'\to u)J(x,u')\,du',\end{aligned} \tag{5}$$

where $J(x,u)$ is the differential neutron current, u is the neutron lethargy defined as $\ln(E_0/E)$, $\Sigma_{s0}(u'\to u)$, and $\Sigma_{s1}(u'\to u)$, are the isotopic and anisotropic components of the differential scattering cross section [9]. S_0 is defined by Equation 6,

$$S_0(x,u) = \int_0^u \Sigma_{in}(u'\to u)\phi(x,u')\,du' + S_{ext}(x,u), \tag{6}$$

where $\Sigma_{in}(u'\to u)$ is the inelastic scattering contribution and $S_{ext}(x,u)$ is the contribution of the D-T neutron generator as the source of neutrons.

Due to the energies of the incident source neutrons being much greater than 1 MeV, s-wave scattering is not valid and p-wave scattering is necessary to accurately describe the system. It is convenient to write Equation 5 in terms of slowing down densities defined by Equation 7,

$$\begin{aligned}q_0(x,u) &= \int_0^u \int_u^\infty \Sigma_{s0}(u'\to u'')\phi(x,u')\,du''\,du',\\ q_1(x,u) &= \int_0^u \int_u^\infty \Sigma_{s1}(u'\to u'')J(x,u')\,du''\,du'.\end{aligned} \tag{7}$$

To find a solution for $\phi(x,u)$ requires solving approximate differential equations for $q_0(x,u)$ and $q_1(x,u)$, which relies upon the continuous slowing down approximation shown as Equation 8,

$$\begin{aligned}\lambda_0 \frac{\partial q_0}{\partial u} + q_0(x,u) &= \beta_0 \phi(x,u),\\ \lambda_1 \frac{\partial q_1}{\partial u} + q_1(x,u) &= \beta_1 J(x,u),\end{aligned} \tag{8}$$

where $q_0(x,u)$ and $q_1(x,u)$ can be described by Equation 9 after performing a Taylor expansion on $\Sigma_{s0}(u' \to u)\phi(x,u)$ from Equation 7 about $u = u'$,

$$\begin{aligned}q_0(x,u) &= \xi \Sigma_s(u)\phi(x,u) + \frac{a}{\xi}\frac{\partial}{\partial u}\left[q_0(x,u)\right],\\ q_1(x,u) &= \zeta \Sigma_s(u) J(x,u),\end{aligned} \tag{9}$$

where ξ and a are defined as,

$$\begin{aligned}\xi &\equiv 1 - \alpha \frac{\ln \frac{1}{\alpha}}{1-\alpha},\\ a &\equiv \alpha \frac{\left(\ln \frac{1}{\alpha}\right)^2}{2(1-\alpha)} - \xi.\end{aligned} \tag{10}$$

Additionally, ζ is defined as,

$$\zeta = \frac{(1+\gamma)^2}{\gamma^2}\left[\frac{1+\gamma}{9}\left(1 - \alpha^{3/2}\left(\frac{3}{2}\ln\frac{1}{1+\alpha}\right)\right) - (1-\gamma)\left(1 - \alpha^{1/2}\left(\frac{1}{2}\ln\frac{1}{1+\alpha}\right)\right)\right], \tag{11}$$

where $\gamma \equiv A^{-1}$, which is the inverse of the mass number of the moderator of interest for $A \gg 1$. Describing $q_0(x,u)$ and $q_1(x,u)$ in this fashion is called the *consistent* P_1 *approximation* and upon solving for $\phi(x,u)$ describes the differential neutron flux in both space and energy to use in Equation 4. This approximation relies heavily upon the moderator being a heavy mass and weakly absorbing system, in which graphite is a perfect example of this type of moderating medium.

Equation 4 only models the total neutron absorption reaction rate, and does not include the subsequent radiation emission upon neutron capture or the response of the detector to the emitted radiation. The radiation emitted is dependent solely on the isotope and the neutron interaction of interest. Neutron activation analysis is based primarily on Equation 4, but is difficult to evaluate even under approximate conditions like the P_1 *approximation* above. Additional simplifications are necessary, including discretization of space and energy to model complex geometries and neutron cross sections. This forces the use of deterministic or stochastic radiation transport codes such as ones that rely on Monte Carlo, which can accurately model these scenarios. This is done in Chapter 5 where the experimental results are compared to those simulated by MCNP.

The gamma response from the detector is the only quantity of interest for neutron activation analysis and not only relies upon the neutron absorption cross section of a given isotope, but also the branching ratio and branching fraction of the activation product to the daughter products. The branching fraction is defined as the fraction of nuclei which decay by an individual decay mode with respect to the total number of nuclei which decay. The branching ratio is defined as the fraction of gamma rays emitted by an individual decay mode. The time rate of change of the radionuclide concentration is described by

$$\frac{dN(t)}{dt} = -\lambda N(t) + V \int_0^{t_1} \int_0^{\infty} N_{\text{Target}}(t)\sigma_a(E)\phi(E)\,dE\,dt', \tag{12}$$

where N_{Target} is the number density of the target nuclei, $N(t)$ is the number density of the activation product, $\sigma_a(E)$ is the differential neutron absorption cross section, $\phi(E)$ is the differential flux, t_1 is the duration of irradiation by the neutron generator, and V is the volume of the target. The steady state solution shown below is "saturated activity" or $t >> t_{1/2}$

$$N(t = t_{sat}) = \left(1 + \frac{\lambda}{V\int_0^{\infty}\sigma_a(E)\phi(E)\,dE}\right)^{-1}. \tag{13}$$

However, saturated activity is not a requirement because Equation 12 can be solved analytically without the assumption of steady state. For In-116 and Pd-109 saturated activity was not achieved before transporting the sample from the neutron generator to the detector station. Thus, the solution to the differential equation after manipulation and without the assumption of saturation can be written as

$$N(t) = \left(\mathrm{e}^{x(\mathrm{t}_1 - t)} - \mathrm{e}^{-xt}\right)(x - \lambda), \tag{14}$$

where x is a parameter given by

$$x = \lambda + V \int_0^{t_1} \int_0^{\infty} \sigma_a(E)\phi(E)\, dE\, dt'. \tag{15}$$

For short-lived nuclides the time constants, ($\lambda \equiv \ln 2/T_{1/2}$ and $T_{1/2}$ is the half-life of the isotope of interest), are relatively large and saturated activity can be achieved in very short time periods. This is beneficial in environments where the neutron source can be depleted and in low-flux environments. However, in high-flux environments the decay of these short-lived is very rapid and detector dead-time must be taken into account.

After the target is transported from the neutron source the production term vanishes and this reduces to Equation 17 with the initial condition $N(t = t_1) = N_1$ where t_1 is the duration of neutron flux exposure. The resulting equation is,

$$\frac{\mathrm{dN(t)}}{\mathrm{dt}} = -\lambda N(t), \tag{16}$$

where the solution of the differential equation can be written as,

$$N(t) = N_1 \mathrm{e}^{-\lambda t}. \tag{17}$$

The combination of Equations 14 and 17 in their respective time frames yield the curves shown in Figure 3. Figure 3 shows the isotope activity as a function of time when the sample is cyclically activated. Additionally, the quantities t_w and t_c are the transport or wait time and the counting time respectively with the expectation that $t_w << T_{1/2}$. The longer the pneumatic transport system takes to transport the irradiated sample from the source to the detector, the less time the detector has to measure the radioactive daughter products before decay.

As suggested by Sterlinski, Equation 17 is well suited to apply a linear least squares process to determine the decay constant λ and the initial activity. It is preferential to perform a weighted least squares fitting to the natural log of Equation 17. Reducing the background radiation from cosmic rays, naturally occurring background sources, and the neutron generator is a necessity in making the detection of short-lived activation products possible by increasing the signal to noise ratio.

Transporting the sample away from the neutron source and into a well shielded environment can reduce the background term by orders of magnitude and is easily achievable with a pneumatic transfer system in a reactor environment or in a pulsed neutron facility. This will be discussed in further detail in the next chapter.

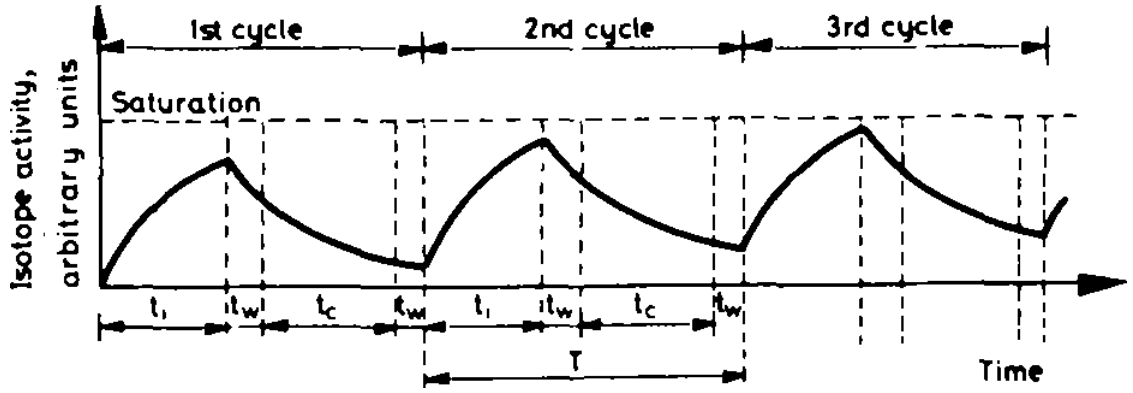

Figure 3: Isotope Activity versus Time Under Cyclic Activation [7]

CHAPTER 3: SYSTEM DESIGN

The goal of this thesis is to construct and benchmark a pneumatic transport system to detect short-lived activation products. A ThermoFisher P-385 D-T neutron generator will be utilized as the source for incident neutrons to actively interrogate the target materials of interest. The radiation to be detected are delayed gamma rays from the decay of the activation product to the daughter products after transportation. The expectation is the sample must be transported from the source to the detector within a fraction of the half-life of the activation product for this system to be successful. The gamma detector chosen for the experiment is high-purity germanium (HPGe) over other choices due to the excellent energy resolution.

To design a successful pneumatic transport system to run the experiments in the next chapter, the transport system must exhibit the following characteristics; the ability to transport sample vials consistently, to transport samples much faster than the half life of the target being interrogated, and to interface with other external systems such as the neutron generator digital control box and the digital spectrometer attached to the HPGe detector. These criterion are very similar to the recommendations of Kreiner and Paas and Sullivan in the literature review [3] [4]. Semiconductor detectors, including high-purity germanium, are very sensitive to neutron damage and cannot be exposed to the relatively intense neutron flux present within or near the graphite pile. By separating the source from the detector, the background radiation can also be reduced by enclosing the detector in lead. Thus, the purpose of the pneumatic transport system described in this chapter is not only to measure short-lived radioisotopes effectively, but also to protect the detector. The pneumatic transport system can be separated into three major components, the physical system which consists of piping, valves, and the laser and photo detector configuration, external systems (neutron generator and the detector assembly), and the control system. Figure 4 shows the top level schematic of the entire piping network, valve placements, and laser-diode assembly.

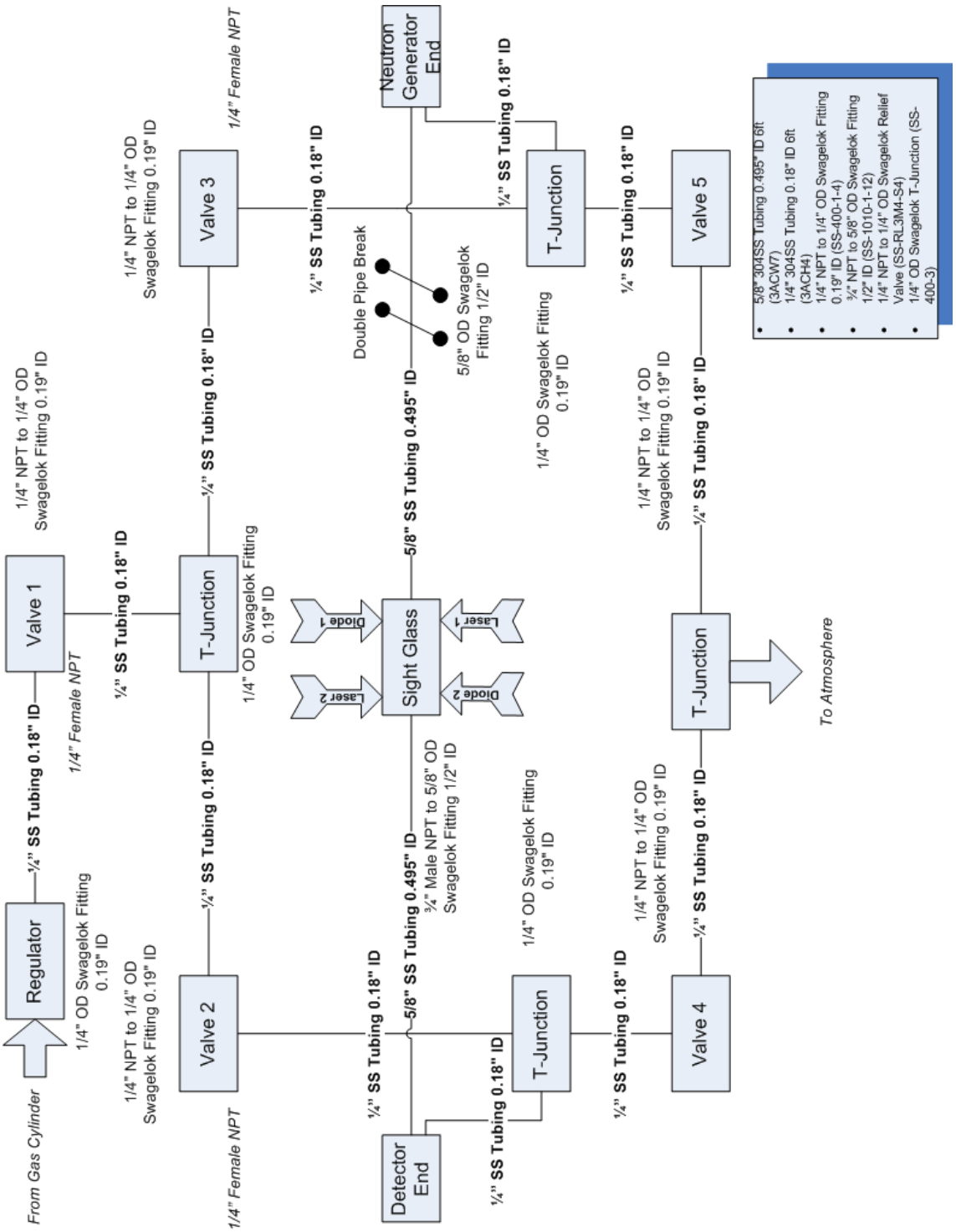

Figure 4: Top Level Schematic for Pneumatic Transport System

3.1 TRANSPORT SYSTEM DESIGN

The physical portion of this system, shown in Figure 4 consists of the transport tube, the two end-caps, the inlet/outlet lines, and the piping network for the solenoid valves that control the direction in which the sample vial will move. The design choice of the size of piping was based on the transport system built by Paas and Sullivan discussed in the literature review [4]. The material chosen for the pneumatic transport system was stainless steel due to its strength, durability, and ease of welding/brazing. The only downside with using stainless steel is the activation of stainless steel; however, there has been no indication of any significant activation within any component, unlike what would be common if this system was to be built at a research reactor. Using the schematics of Paas and Sullivan, similar sizing of transport tube and gas inlet/vent tubing were applied to this installation as it was the smallest diameter tubing which could achieve quick transport times with relatively low pressure input [4]. The pressure can be scaled up to increase the sample vial speed required based on the half-life of interest.

The placement of the end-caps must be at the nose of the neutron generator at one end and housed within a detector shield on the other end. The restrictions on the detector end of the system were less stringent, but the goal was to achieve maximum geometric efficiency. Thus, the detector must be as near to the target material as possible. Figure 5 shows the configuration of the end-cap built for the detector and neutron generator side. This required the construction of end-caps that have all connections (transport tube and inlet/vent tube) connected on the side.

The entire system was constrained to 150 psi by the Pyrex sight glass, but typically operated between 30 psi and 50 psi. Based on the mass of the sample vial (up to ten grams) the sample vial can easily reach the other side in less than a second consistently at an inlet pressure of 40 psi.

Figure 6 shows the piping network that was constructed to allow for argon gas to flow in either direction and for the vent. The simplest construction would rely on a four valve network (two inlets and two vents); however, due to concerns originally of cycling the inlet valves too frequently,

an extra valve was added at the inlet from the regulator outlet.

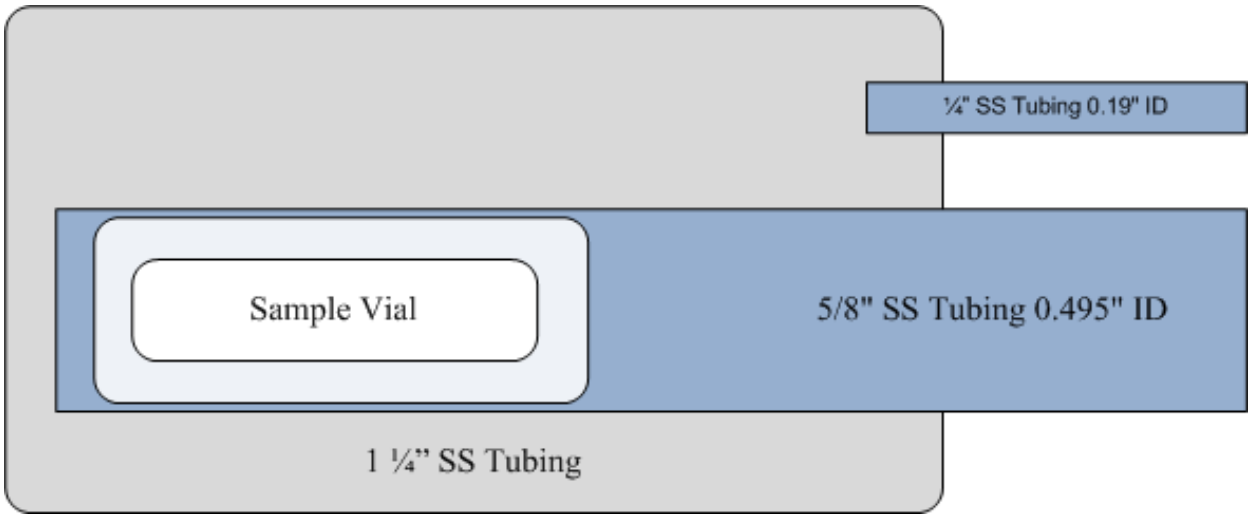

Figure 5: End Cap Schematic for Pneumatic Transport System

3.2 PHOTODETECTOR ASSEMBLY

The measurement of the velocity and deceleration of the sample required the installation of a photo detector assembly to measure the time elapsed as the vial traveled from the neutron source to the detector. Additionally, the assembly and location necessitated the installation of a inline sight glass with the transport tube to pass laser light. None of the work previously discussed in the literature mentioned how the transport time was measured from their source to detector. This required the design of a photo detector system that produced a clean and consistent signal. The sight glass was made to 5/8 inch outer diameter and 1/2 inch inner diameter, which is the same as the transportation tube to allow for the vial to move freely. Pyrex was chosen over many other materials, such as quartz, due to its high transmittance of light in the 865 nm range (over 90 percent). The wavelength of the lasers in the photo detector assembly are the most sensitive to light near 865 nm. With respect to the literature, it is believed that this experimental assembly is the only photo detector system as the means of determining the transport time of the sample vial.

To measure the quantities mentioned above, two 865 nm infrared lasers and two photo diodes spaced approximately five inches apart were used to capture the sample as it moved through the

sight glass. Figure 7 shows the two laser and photo diode pairs in their positions relative to the sight glass.

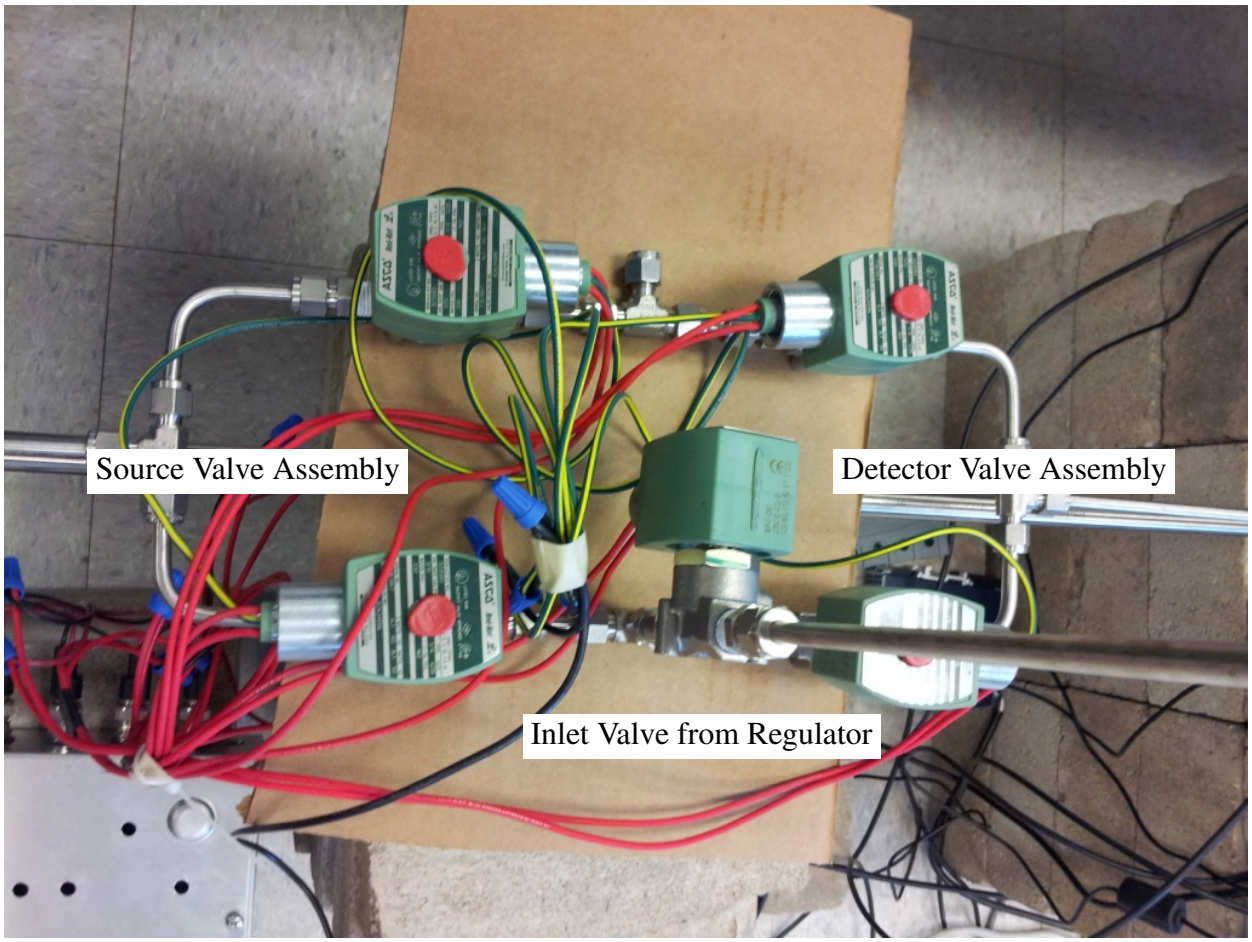

Figure 6: Argon Valve Control Network

Using this combination, the ultimate goal was to measure the elapsed time the sample vial blocked each laser beam as the sample vial passed from the neutron generator to the HPGe detector. The output of the photo detectors are transistor-transistor logic outputs and output an inverted square wave when the photo diode is blocked by the sample vial. Using the inverted square wave outputted by the photo detectors allows for the time that the sample vial blocks each laser-diode pair. Using one-dimensional kinematics, it is possible to determine the velocity across each laser-diode pair and the deceleration of the sample vial as it travels between to the two laser-diode pairs as it passes through the transport tube on its way to the detector station.

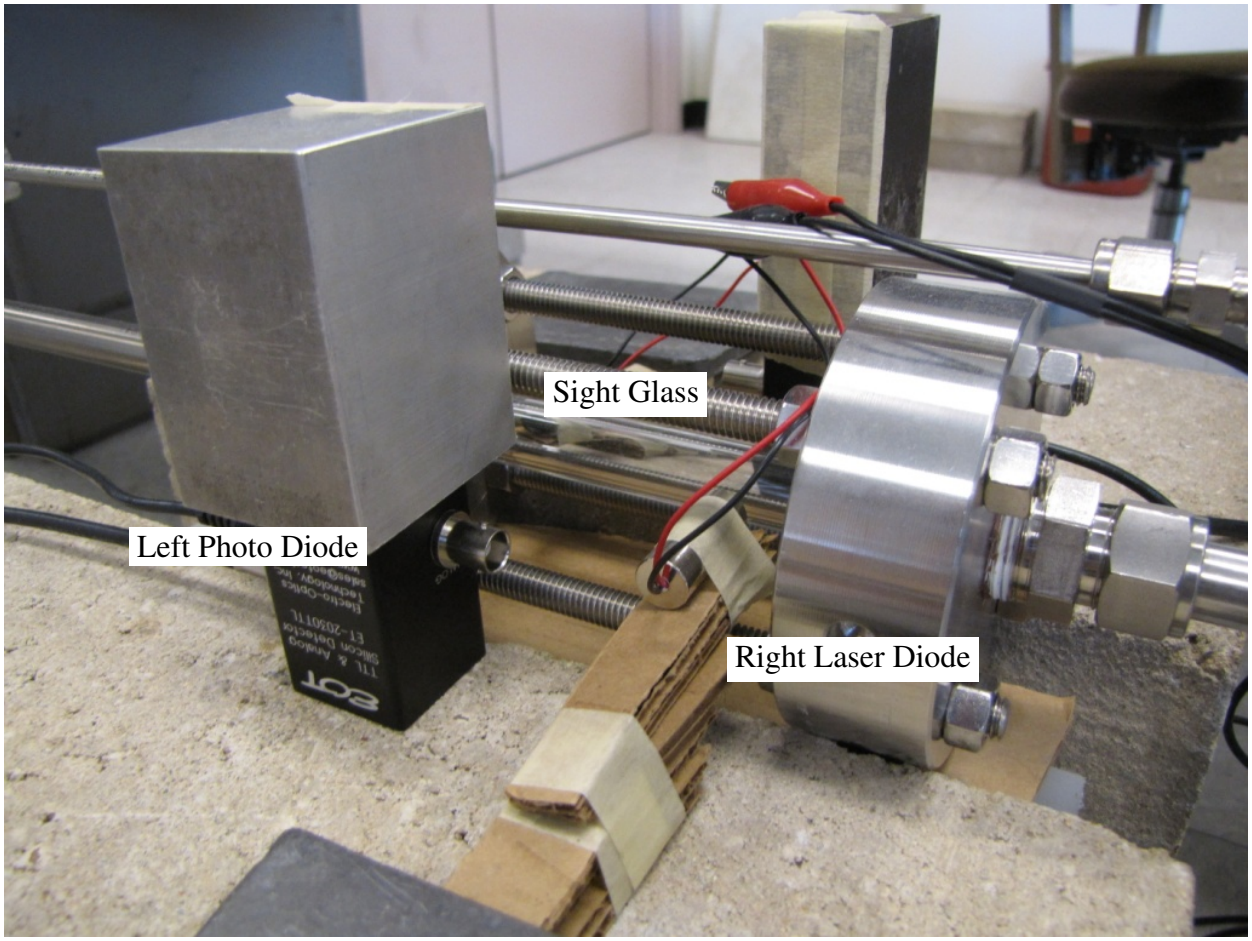

Figure 7: Sight Glass With Laser and Photodiode Assembly

Equation 18 shows the system calculation of the deceleration of the sample using the output of the photo detector,

$$a = \frac{\Delta x}{t_b}\left(\frac{1}{t_2} - \frac{1}{t_1}\right), \tag{18}$$

where Δx is the distance between the two photodetectors, t_1 is the time the sample vial blocks the photo detector closer to the neutron source, t_2 is the time the sample vial blocks the photo detector further from the neutron source, t_b is the time elapsed to move between the two photo detectors, and a is the deceleration of the sample. The timing to start the gamma detector uses the deceleration computed from Equation 18 and the remaining length of transport tube before the gamma ray

detector. Due to the short distances, Equation 19 is an approximation; using one-dimensional kinematics, assuming constant deceleration, the sample arrival time at the detector station is given by,

$$t = \frac{1}{|a|}\left(v_2 + \sqrt{v_2^2 + \frac{|a|L}{2}}\right), \tag{19}$$

where v_2 is the velocity of the sample vial as it crosses the downstream photo detector closer to the gamma detector, $|a|$ is the magnitude of the acceleration calculated in Equation 18, L is the length of pipe between the photo detector to the gamma detector, and t is the time shift necessary to start the detector when the sample arrives. Table 2 shows the an example of timing related information recorded by the control system to calculate the velocities and the deceleration for one of the indium trial runs. In Table 2, the "front diode" is considered the photo diode nearest to the neutron generator, the "rear diode" is considered the photo diode furthest from the neutron generator, and the run counter is the cycle number where the pneumatic transport system transfers the sample from the neutron generator to the detector for counting.

Excluding the pneumatic transport system, two other independent systems must interact with the control system. These two systems are Ortec digital gamma spectroscopy system (DSPEC) and the ThermoFisher P-385 control box. The requirements of these connections are to command the DSPEC to start acquisition, to inform the valve control system that acquisition has completed, and to send the sample to the neutron source. Using the DSPEC in a way similar to a sample changer allowed the use of simple TTL logic to signal the DSPEC when to start taking a spectra through the "Sample Ready" input and to signal the control system when to send the sample vial through the "Change Sample" output.

The control box of the neutron generator was far more reasonable to manage with the control system than the DSPEC due to a simple TTL input and output with no need for a serial connection

Table 2: Photo diode Timing Information for Use With Equation 19

Run	**Front Diode Time** (ms)	**Rear Diode Time** (ms)	**Source to Destination** (ms)
1	6.104	6.162	673.2
2	7.569	7.507	678.5
3	6.512	6.246	677.2
4	8.186	7.735	670.2
5	6.246	6.267	692.9
6	5.940	5.981	674.3
7	6.296	6.368	675.1

to the control system. However, the digital control box of the neutron generator still required a serial connection to the computer to put the neutron generator in standby mode with active high switch control. This allowed the control system to signal to the control box of the neutron generator to start the production of neutrons.

Standby mode can be best described simply as a setting that maintains the operating voltage at a user-defined value and switches between a user-defined current to a minimal current to control the neutron output of the generator. This mode allowed for the ability to control when the neutron generator was producing neutrons with a logic high over the TTL input (when the sample vial was in graphite pile) and when it was not with a logic low over the TTL input (when the sample vial leaves the graphite pile and is at the detector station). The maximum neutron output of the neutron generator is 3.5×10^8 neutrons per second.

National Instruments products were chosen to control all signaling between the external systems and operation of the valves to operate the pneumatic transport system with minimal user intervention. Residing in the CompactRIO is a real-time microprocessor based on the PowerPC architecture and a Xilinx Spartan III XC3-S2000 FPGA. Building this system relied on the programming of both devices within the CompactRIO using two different languages. The microprocessor was programmed graphically in NI LabVIEW 2012; and for the Spartan III, a custom hardware implementation was produced in VHDL and integrated with the LabVIEW code.

The control system had the following options installed to signal the other hardware: a LVTTL

digital input/output module to handle signaling and receiving signals from the DSPEC and the neutron generator control box, a digital output module to drive the solid state relays that open the valves, and an RS-232 module to communicate with the DSPEC over serial.

Figure 8 shows the state machine diagram that was implemented in VHDL. The FPGA portion of the control system was written in VHDL using Xilinx ISE 14.2 and was incorporated using the LabVIEW FPGA 2012 module so it could be used on the CompactRIO. The VHDL portion of the project itself is not very complicated as it can be broken down into two fundamental components. The first component is the valve control finite state machine and the second component is what measures the blockage times as the sample vial passes the photo detectors. This is so the real-time processor on the CompactRIO can calculate the velocities across the two laser-diode pairs and the acceleration between the two pairs. The complete VHDL source code is included in Appendix I. Using Xilinx's ISim, the complete system had been tested as if the real hardware was running; albeit, not in real time. The terminology being when a device is outputting less than 0.8 V the logic level is considered a low and when a device is outputting more than 2 V the logic level is considered a high. A logic high is initiated on the start signal the system responds by cycling the valves so the sample can move to the source, waits for a user-controlled time, and initiates a high on the source signal. After reaching the user-defined time limit for irradiation, the control system sends back the sample by cycling the valves to allow gas to flow in the opposite direction. While the valves toward the detector side are open, the control system starts a counter to record, in clock cycles, the total transport time from when the sample leaves the source to when it reaches the second photo diode. The control system then waits for the vial to block the pair of photo diodes and counts how many clock cycles each photo diode is outputting a logic low.

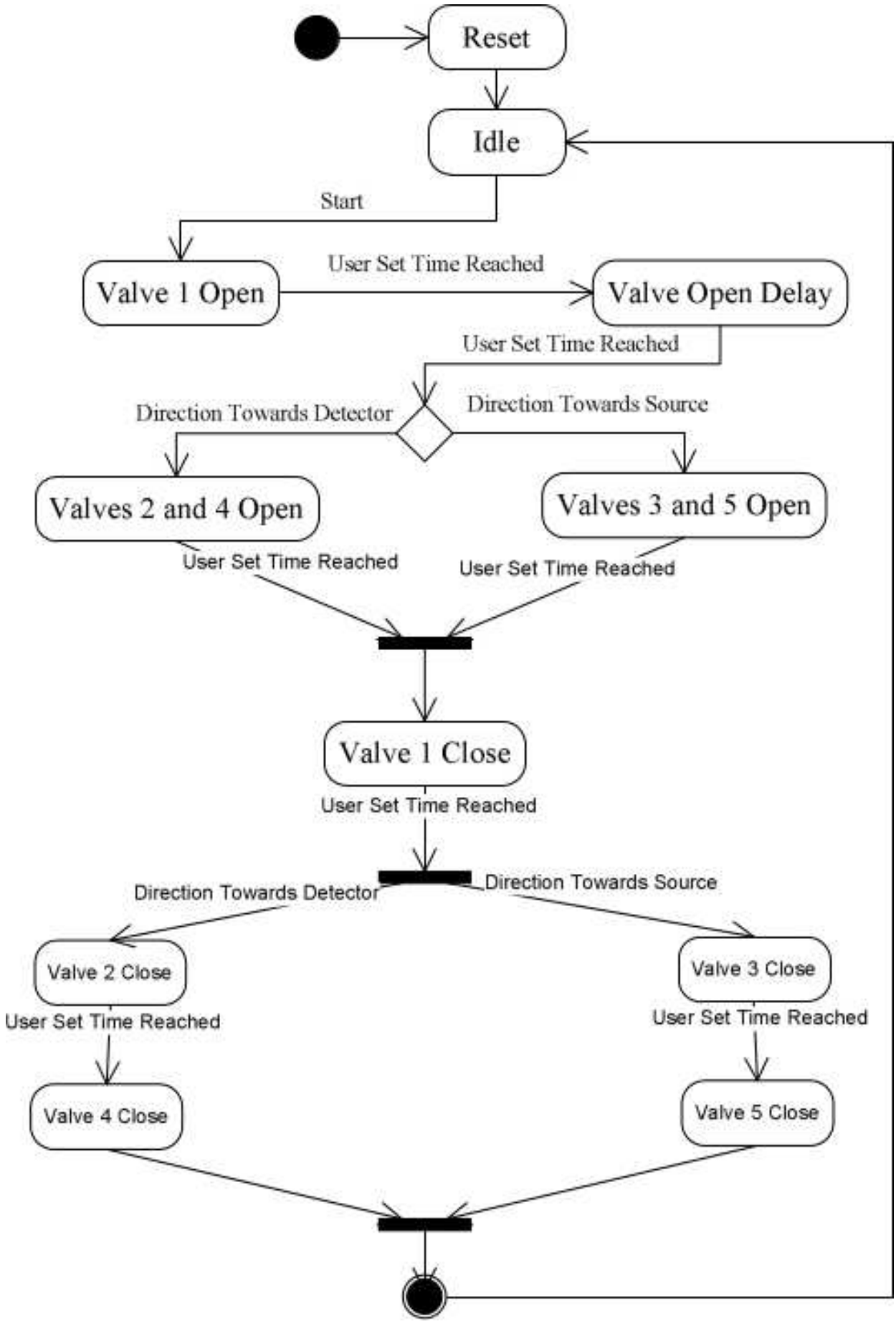

Figure 8: State Diagram Implemented in VHDL for Valve Control Operation

When the second photo diode returns to the unblocked state, the control system stops the counter recording the total transport time in clock cycles and the ”Sample Ready” output is set to logic high. This communicates to the DSPEC that it is time to start the job to record the required amount of spectra defined by the user. The FPGA transfers all counters that stored timing related information to the microprocessor to compute and store the velocity and the acceleration. Once the DSPEC recorded all spectra related to that run, the DSPEC signals the control system that it has finished by asserting logic high through the ”Change Sample” output.

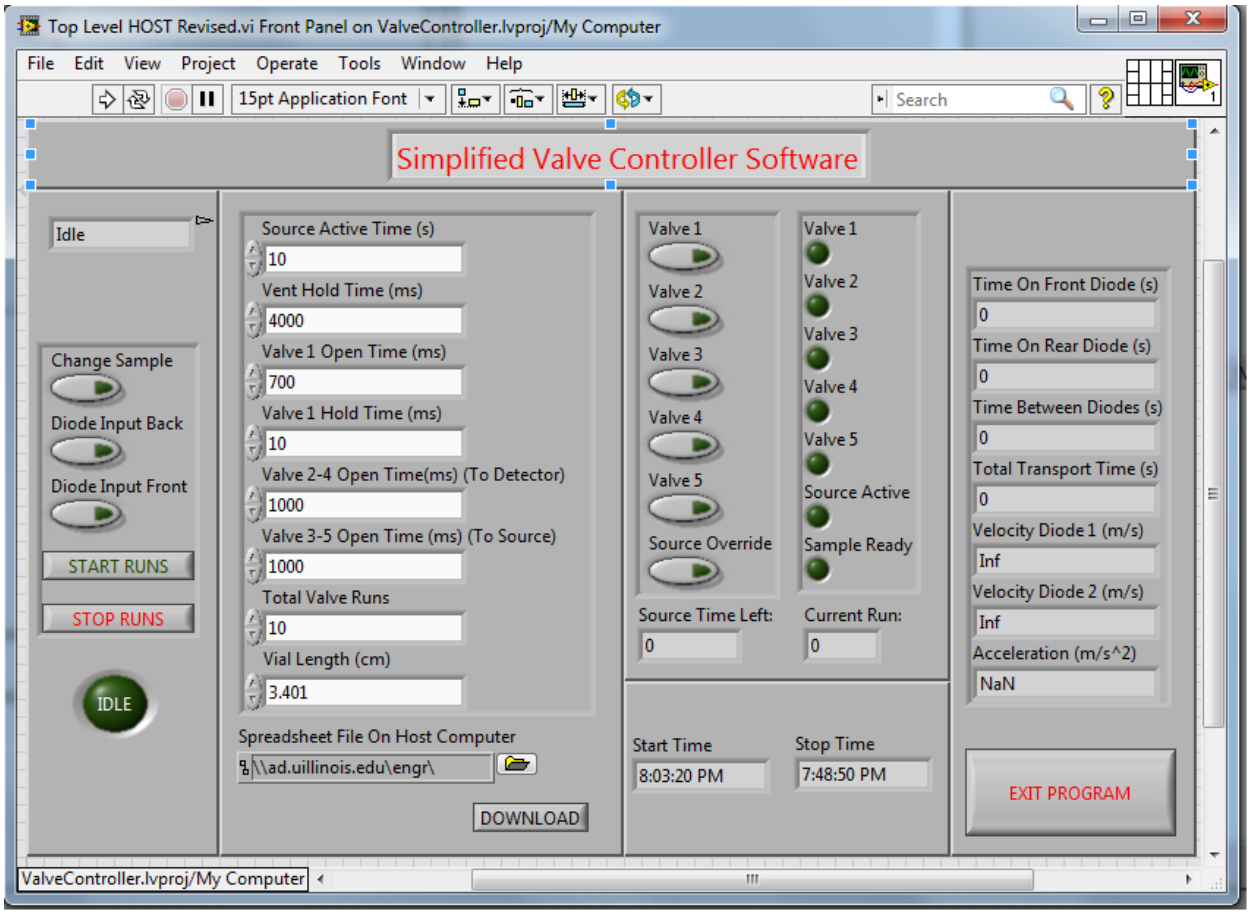

Figure 9: Human Machine Interface for Pneumatic Control System

This starts the process once again from the beginning until the number stored in the internal runs counter is equal to the amount of user-defined runs. Using the FPGA over the real-time processor or the host computer allows for the guarantee that the diode, neutron generator, and

DSPEC signals will be captured and processed in a deterministic manner. This improves the reliability of the system by allowing the system to run even during a computer failure. It also improves consistency since an operating system such as Windows must schedule processes and becomes non-deterministic, but an FPGA can operate in a deterministic manner and does not rely on an operating system at all.

However, the real-time processor of the CompactRIO is still a necessity as it is the bridge between the FPGA and the host computer. The processor also performs simple calculations such as the velocity and the acceleration mentioned earlier in this chapter. The LabVIEW graphical code controlling the real-time processor can be found in Appendix II. The final portion of the control system is the LabVIEW graphical code written for the host computer. Figure 9 below is the human-machine interface (HMI) panel. The only role of the host computer is to tell the control system when to start, to monitor the overall operation of the control system, and to save the spectra generated by Ortec's Gamma Vision to the file system for further analysis.

3.3 DETECTOR ASSEMBLY

Due to the complexity of delayed gamma emission from materials that may be used in the future, the requirement of a detector that has excellent energy resolution, even at the expense of relative efficiency, is paramount. For the experiments presented in the next chapter, an Ortec Pop Top high-purity germanium detector was chosen with a mechanical X-Cooler II. The consequence of using a high-purity germanium for the experiments presented in the next chapter is its relatively low efficiency compared to the lower resolution scintillator detector. The neutron activation experiments discussed in the next chapter were more difficult (because the activation products have well separated gamma ray emission lines).

To reduce the background at the detector station, the detector end cap of the transport tube and the entire detector were wrapped in lead shown in Figure 10. The dimensions of the HPGe that has been used for the experiment was a 2 inch by 2 inch crystal.

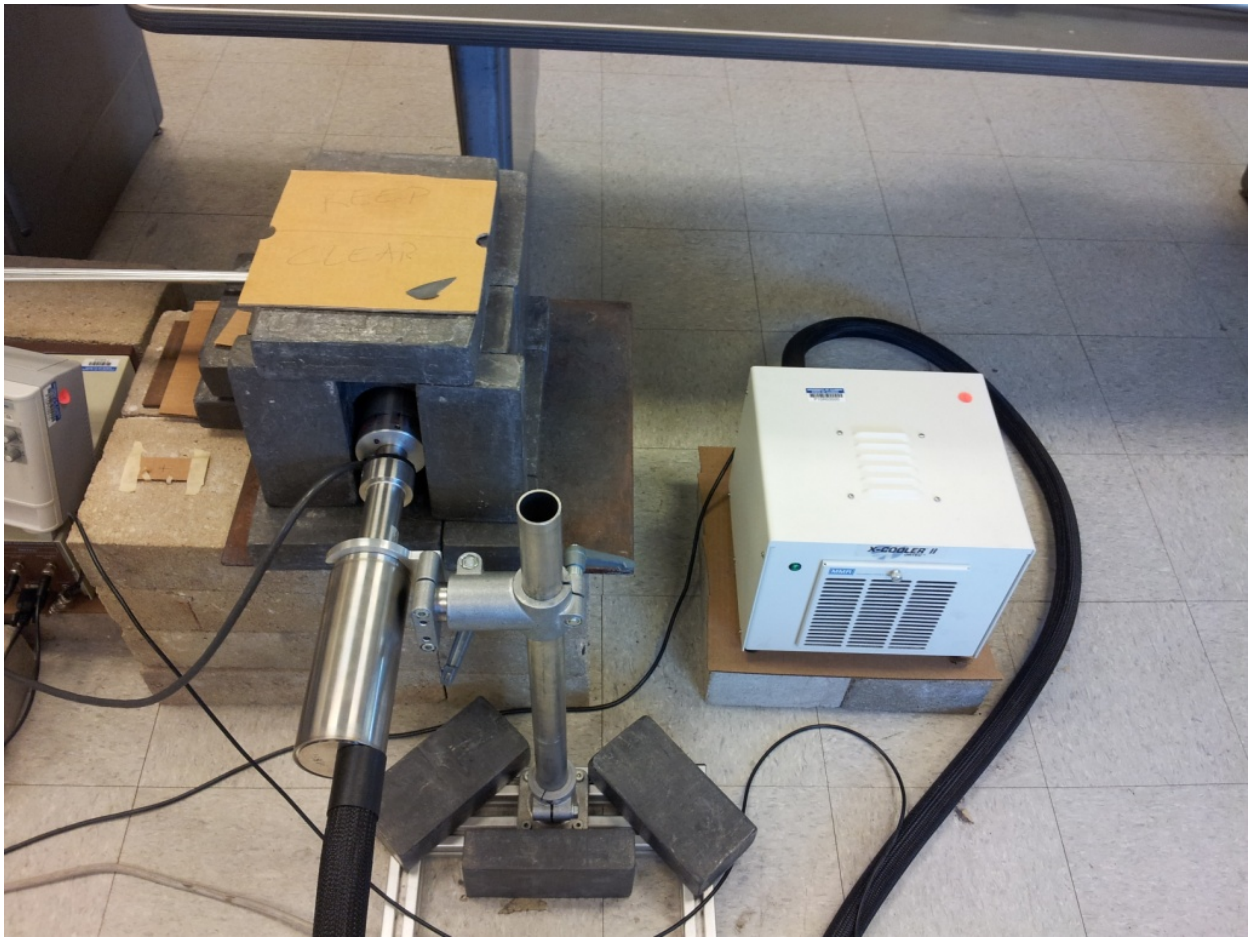

Figure 10: High Purity Germanium Detector Wrapped in Lead Shielding

To calibrate the energy of the high purity germanium system the channel numbers of the digitizer must be correlated to radioisotopes whose gamma ray energies are known. Figure 11 describes the linear correlation between the channel number and the energy using reference sources. Table 3 is the result of the energy calibration using four calibration sources.

Table 3: Energy Calibration of HPGe Detector S/N: 44TP21936B

Source	**Energy** (keV)	**Channel Number**
Barium-133	81.00	629.77
	276.40	2145.42
	302.85	2349.82
	356.01	2765.07
Cesium-137	661.62	5140.22
Manganese-54	834.83	6486.29
Sodium-22	1274.54	9882.23

To accurately calculate the production of the daughter product the energy dependent efficiency in a detector, the branching fraction, and the branching ratio must be characterized.

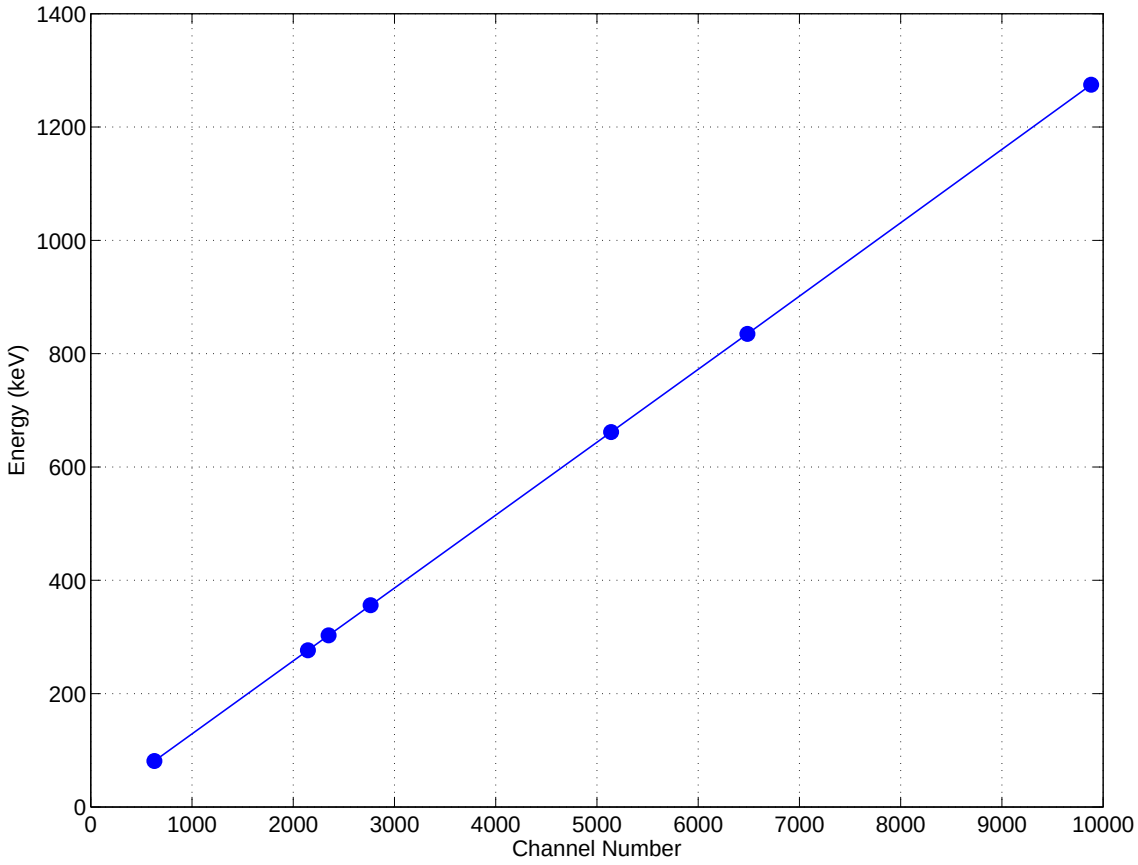

Figure 11: Energy Calibration

To determine the efficiency, one must characterize the geometry and know the current activity of a near-point source. Equation 20 describes the fraction of source events detected, known simply as the detector efficiency, in the detector,

$$S = N\frac{4\pi}{\varepsilon_{ip}\Omega}, \tag{20}$$

where the solid angle, Ω is defined as an integral over the detector surface that is facing the source

defined as,

$$\Omega = \int_A \frac{\cos\alpha}{r^2}\, dA. \tag{21}$$

The quantity Ω is typically extremely difficult to compute beyond very simple geometries and requires other methods to determine the detector efficiency in a complex geometry or detector arrangement [10]. The geometry of the sample vial is more complex than point-source geometry and is more difficult to calculate the solid-angle subtended for the detector assembly to determine the absolute efficiency, but an alternative method can be used to determine the efficiency. Sealed calibration sources were used to calculate the efficiency outside of the transport system. The germanium detector was placed seven inches away from the each of the calibration sources where point-source geometry was applicable and Equation 22 was used to compute Ω,

$$\Omega \approx \frac{A}{d^2} = \frac{\pi a^2}{d^2}, \tag{22}$$

where A is the surface area of the detector, d is the distance between the source and the detector, and a is the radius of the detector face. Using Ω calculated from Equation 22, it is now possible to calculate $\varepsilon_{ip}(E)$ shown in Table 4 for the detector in point-source geometry.

This allows for the ability to compute the absolute activity built up in the target sample after irradiation given the response of the detector and the solid angle subtended,

$$\ln\varepsilon(E) = \sum_{i=1}^{N} a_i \left(\ln\frac{E}{E_0}\right)^{i-1} \text{[10]}. \tag{23}$$

This data can be fit with a fifth order polynomial and interpolated over the entire energy range of interest, shown in Figure 12. The a_i's and E_0 are the fitting parameters to fit the efficiency as a function of energy.

Table 4: Efficiency Calibration of HPGe Detector S/N: 44TP21936B

Source	**Energy** (keV)	**Efficiency**
Cobalt-57	122.07	0.028789
	136.43	0.034037
Sodium-22	511.00	0.017950
	1274.54	0.0051414
Cesium-137	661.62	0.0086374
Manganese-54	834.83	0.0069279

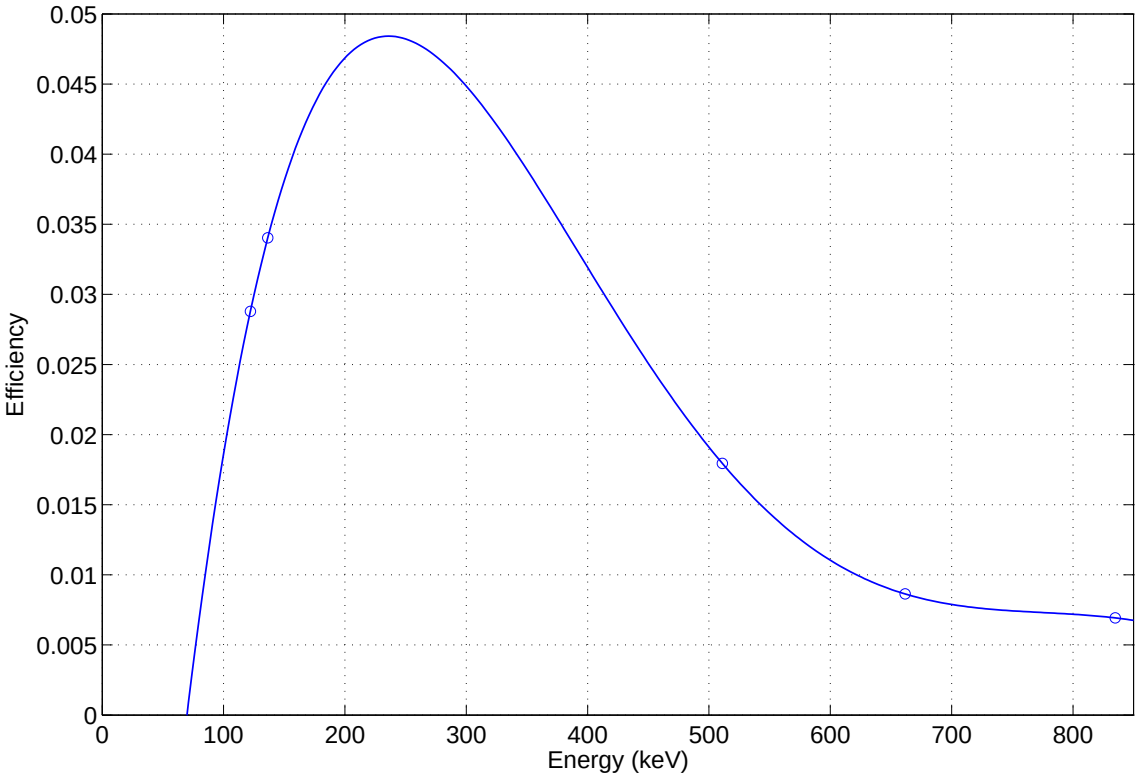

Figure 12: Efficiency Calibration Fit with Equation 23

The fifth order polynomial fitted to the data in Table 4 is only for the point-source geometry and does not apply for the situation where the detector is next to the pneumatic transport tube. A simple ratio can be applied to determine the change in efficiency from point-source geometry to the new geometry.

Using the neutron generator, a sample vial loaded with indium foil was irradiated for thirty minutes and placed in the same point source geometry outside of the pneumatic transport system where the activity of the foil could be measured. After 1200 s of counting, the measured activity

was 133 Bq. The detector was moved into its final position pictured in Figure 10. The same indium foil used previously was reactivated with the neutron generator for thirty minutes using the pneumatic transport system.

Instead of removing the sample vial from the transport system, the sample vial was transported pneumatically and counted for 1200 s. The new activity in the complex geometry was 663 Bq. The significant increase in activity is because of the significant reduction in the distance between the sample vial and the detector face. Therefore, the ratio of the two activities is approximately a factor of five higher in the complex geometry. Using this information the efficiency curve can be modified in the point-source geometry by multiplying by the product of the ratio just mentioned and the transmission percentage through the stainless steel pictured in Figure 13. Figure 13 shows the transmission as a function of energy through stainless steel. Stainless steel is insensitive to higher energy photons; but, near completely stops all low energy photons, especially less than 100 keV. Many internal conversion processes emit x-rays and very low energy gamma rays. The pneumatic transport system will be unable to detect most, if not all of these photons due to the thicknesses of stainless steel being used.

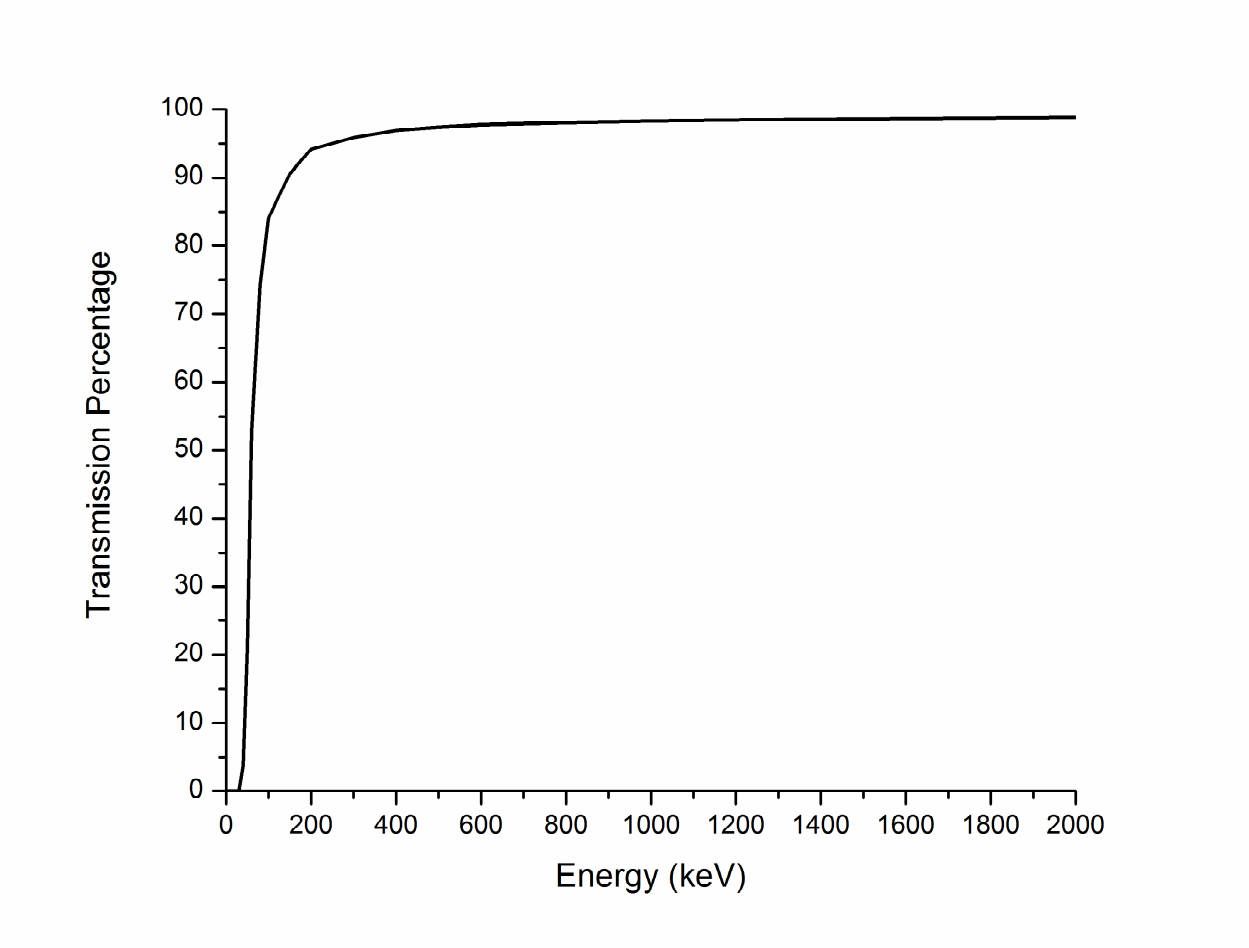

Figure 13: Transmission of Photons Through Stainless Steel

CHAPTER 4: RESULTS

Building upon the mathematical development of Chapter 2 and the experimental design of Chapter 3, in this chapter the results of all experiments will be presented. This chapter will present the half lives measured from the high-purity gamma detector assembly described in the previous chapter and the relevant procedural information during experimentation. Additionally, properties of the individual target materials will be discussed in further detail. Table 5 summarizes the irradiation and counting information in addition to the sample transport times.

Table 5: Quantities Related to Irradiation of the Target Materials

Properties	**Pd-109**	**Pd-107**	**Ge-75**	**In-116**
Source Strength (neutrons/s)	5E7	5E7	6E7	6E7
Transport Time (ms)	711	711	685	650
Error in Transport Time (ms)	3.3	3.3	1.8	1.5
Number of Irradiations	3	25	18	1
Irradiation time per Run (s)	900	300	320	900
Number of Spectra	30	16	18	16
Detector Acquisition Time per Irradiation (s)	120	48	80	30

When plotting on a log-linear scale and fitting Equation 24 to each data set, the y-intercept is the initial activity and the slope is half-life using,

$$\ln N(t) = \ln N(t=0) - \lambda t. \tag{24}$$

For each experiment, a set of gamma spectra were generated as a function of time where time zero is the arrival at the detector from the neutron generator and where each data point is the energy integrated peak for a time t in accordance with suggestions by Sterlinski described in detail in Chapter 2 [8]. Table 6 describes the neutron absorption cross sections for the isotopes of interest as a function of incident neutron energy.

Before each experiment a measurement was taken to subtract the background from each gamma

spectrum collected. Figure 14 shows the room background during one of the experiments as a reference. Suppression of the background in the experiments is essential due to the low quantities of activation products that are achievable with the neutron generator as it improves the signal to noise ratio significantly [7].

Using error propagation, Equation 25 shows the significance of the background term B with respect to the source count rate described by S,

$$\sigma_s = \left(N_{Runs} \times T_{S+B} - \frac{B}{T_B} \right) \frac{\sqrt{\frac{S+B}{(N_{Runs} \times T_{S+B})^2} + \frac{B}{T_B^2}}}{S+B}, \tag{25}$$

where σ_s is the error in the count rate S from the detector configuration, N_{Runs} is number of irradiation and counting cycles, T_{S+B} is the spectra acquisition time with the background, B is the background counts taken without the source, and T_B is the acquisition time with the background alone. The error in the time is not included in σ_s because it is a necessary condition stated previously in this chapter that the transport time must be much much less than the half-life of the radionuclide of interest. For all isotopes presented, the transport time will be less than one second and the half-lives of the each radioisotope will be more than twenty seconds.

In the limit where B goes to zero, Equation 25 becomes,

$$\sigma_s = \frac{\sqrt{S}}{S}. \tag{26}$$

Equation 25 was used as the weighting term for the least squares fitting and is shown as the error bars for each of the least squares fitting results.

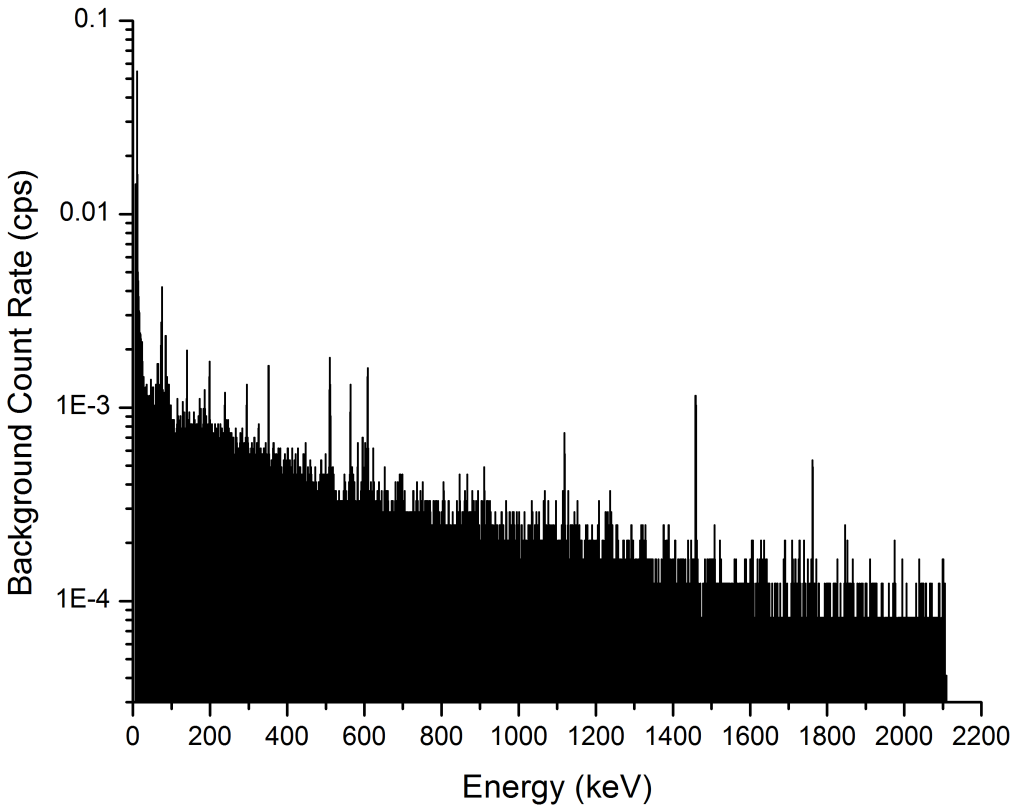

Figure 14: Background Count Rate versus Energy inside Lead Shielding Apparatus

A sample vial was loaded with indium wire into a Lexan sample vial to test the activation performance of the neutron generator. It was also important to test the reliability of the entire system and determine whether or not a system failure could occur during the palladium and germanium tests. This result was expected due to indium-116 not being a short-lived nuclide and having a very large thermal neutron absorption cross section. Figure 15 shows the spectra gathered from the detector after one irradiation run and every gamma ray peak with greater than one percent intensity is clearly visible.

Palladium target material was loaded into a Lexan sample vial for irradiation by the neutron generator. According to the suggestions of Sterlinski, ten to fifteen spectra should be taken per run. The goal of this experiment was to isolate the gamma-ray signature from palladium-109, which is a baseline for the feasibility of detecting isotopes with even shorter half-lives than this. The

half life of palladium 107 and 109 and irradiation information is listed in Table 7. Palladium was chosen over other materials with short half-lives due to the very large resonance absorption cross section in two of its isotopes, as shown in Table 6.

Table 6: Neutron Absorption Cross Sections [2]

Isotope	**Thermal XS**	**Resonance Integral**	14.1 MeV **XS**
Palladium-106 (n,γ)	303 mb	9.288 b	1.123 b
Palladium-108 (n,γ)	8.504 b	252.1 b	1.097 mb
Germanium-74 (n,γ)	150 mb	1.322 b	766.4 µb
Indium-115 (n,γ)	201 b	3208 b	2.944 b

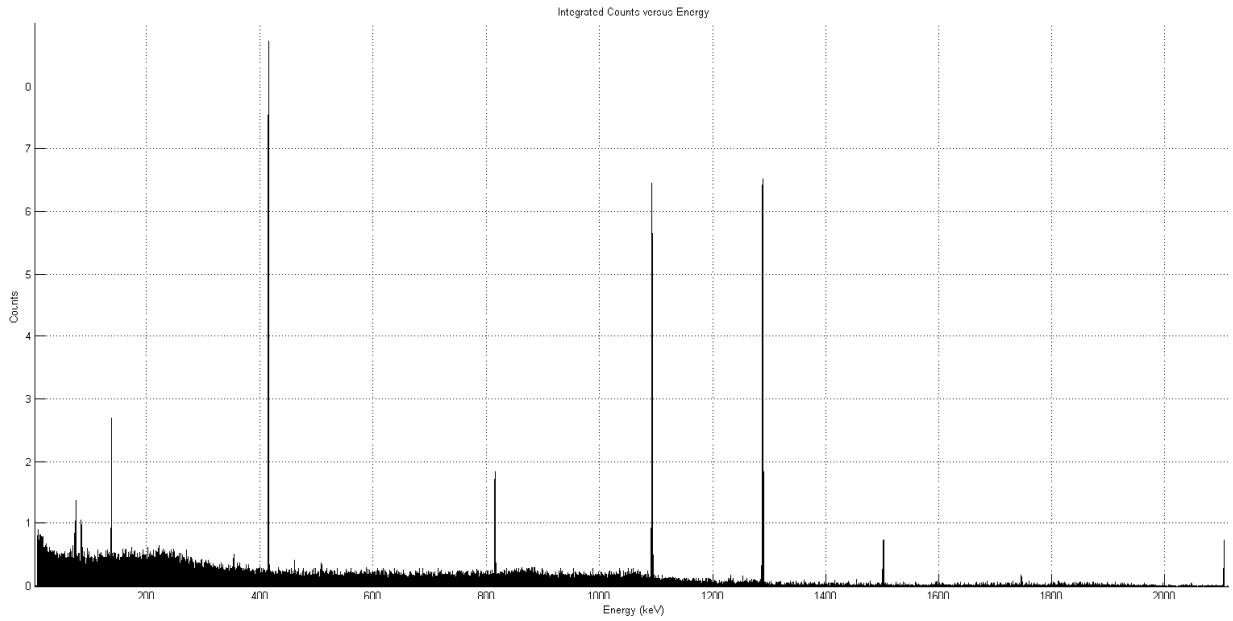

Figure 15: Indium-116 Spectrum

Since this was the baseline measurement, the amount of irradiations to achieve a relative error less than ten percent required three runs. This was not true of the other three isotopes primarily because of the much lower resonance integral with respect to indium-115, shown in Table 6. Also, unlike the indium experiment, the Compton continuum of the highest intensity gammas of the activation products were not visible.

Table 7: Results from Least Squares Fitting from Figures 17, 18, and 20

Quantities of Interest	**Pd-109**	**Pd-107**	**Ge-75**
Published Half-Life (s) [2]	279.36	21.3	47.7
Published Gamma Ray Energy (keV) [2]	214.6	189.9	139.7
Normalized Intensity (Gammas Per Disintegration) [2]	0.687	0.56	0.3936
Error in the Intensity [2]	0.18	0.5	0.5
Experimental Half-Life (s)	279.2	21.8	48.5
Standard Deviation of the Experimental Half Life (s)	27.8	3.7	12.9
Adjusted R-Squared	0.988	0.913	0.823
Experimental Integrated Count Rate (cps)	0.98	1.00	0.58
Experimental Activity (Bq)	47.6	51.0	36.8

To compute the error in the experimental half life, the linear regression line must be computed using two fitting parameters defined by linear least squares such that the residuals from the fit are minimized. These fitting parameters are the slope and the y-intercept where the slope is the decay constant and the y-intercept is the initial activity. The error in the decay constant is taken from the fit itself. The error in the half life is then defined to be,

$$\sigma_T = \frac{\sigma_\lambda}{\lambda} * T_{\frac{1}{2}} \tag{27}$$

where σ_T is the standard deviation in the half life, σ_λ is the standard deviation in the decay constant from the least squares fit, and $T_{\frac{1}{2}}$ is the half life calculated from the fit. Equation 27 is simply the fractional error in the decay constant multipled by the half-life.

The same sample vial of palladium was used and the activation time was increased to five minutes. The neutron generator was run twenty-five times and the detector was run for three seconds, sixteen times each run. The goal of this experiment was to isolate the gamma-ray signature from palladium-107. Palladium-107 also has a much smaller resonance absorption cross section than palladium-109 shown in Table 6. Figure 16 shows the radiative absorption cross section for palladium-109 as an example of the structure of the resonances for each of the nuclides described in this Chapter. For palladium-109, the thermal absorption cross section is on the order of approx-

imately 75 b; whereas, the peak of the resonances is approximately 5000 b. In the presence of sufficient moderation to reduce the energy of the fast neutrons to the resonance region the palladium target will absorb the epithermal neutron. However, the absorption cross section for all of the isotopes in this thesis does not describe the probability of decay to an excited nucleus over the ground state after neutron capture.

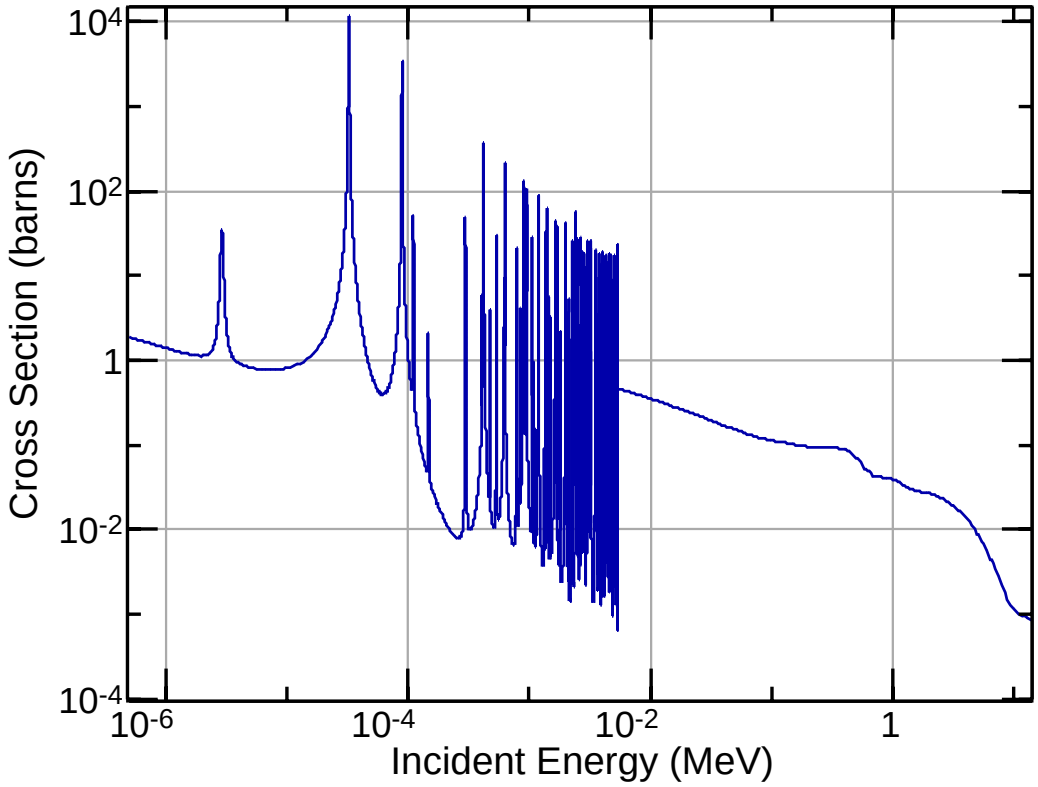

Figure 16: Pd-109 Radiative Neutron Absorption Cross Section [2]

According to Sterlinski, as long as the relative error in the half-life is less than twenty percent, it is expected that the result of the measurement of the half-life to have minimal bias. Though Pd-109 is not necessarily a short-lived half-life according to this thesis or previous researchers described in the literature. There was no expectation of any major difficulties occurring in obtaining a half-life for palladium-109. Thus, it was possible to successfully measure the half-life of Pd-109 to less than ten percent relative error shown in Table 7. The mean transport time was used as the shift from time zero (sample leaves the source) to the time that the sample arrives at the detector.

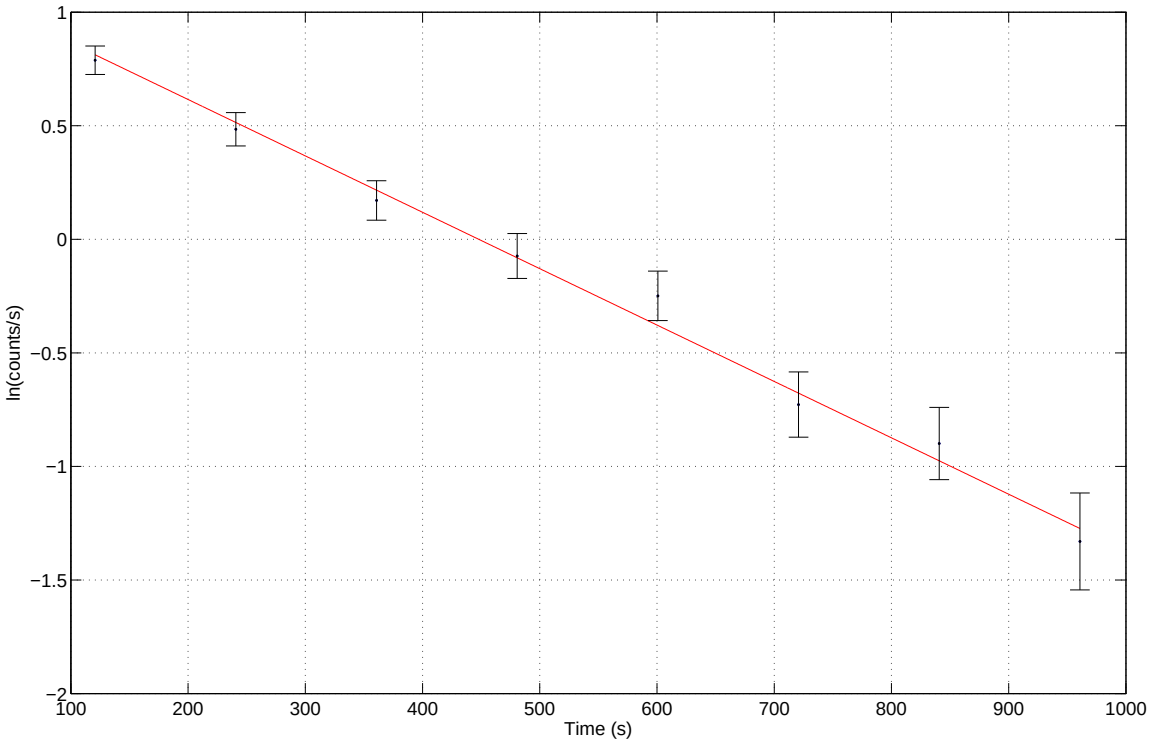

Figure 17: Pd-109 Experimental Half-Life Least Squares Fit

However, palladium-107 is a completely different case since the half-life is about a tenth of palladium-109. To achieve the required statistical accuracy the collection of twenty-five runs of data to achieve a half-life with a fairly large relative error. The neutron generator is running at twenty percent full power, but in comparison the published half-life from the literature has a relative error of about two percent.

Since the target sample did not change from the experiment with palladium-109, the average transport time stayed within the same upper and lower bounds. This was the expected result since the pneumatic transport system has very low variability in the transfer times of the sample vial even after many repeated runs. According to Kreiner, this is essential for any transport system where statistical accuracy in the half-life of short-lived radioisotopes is important [3].

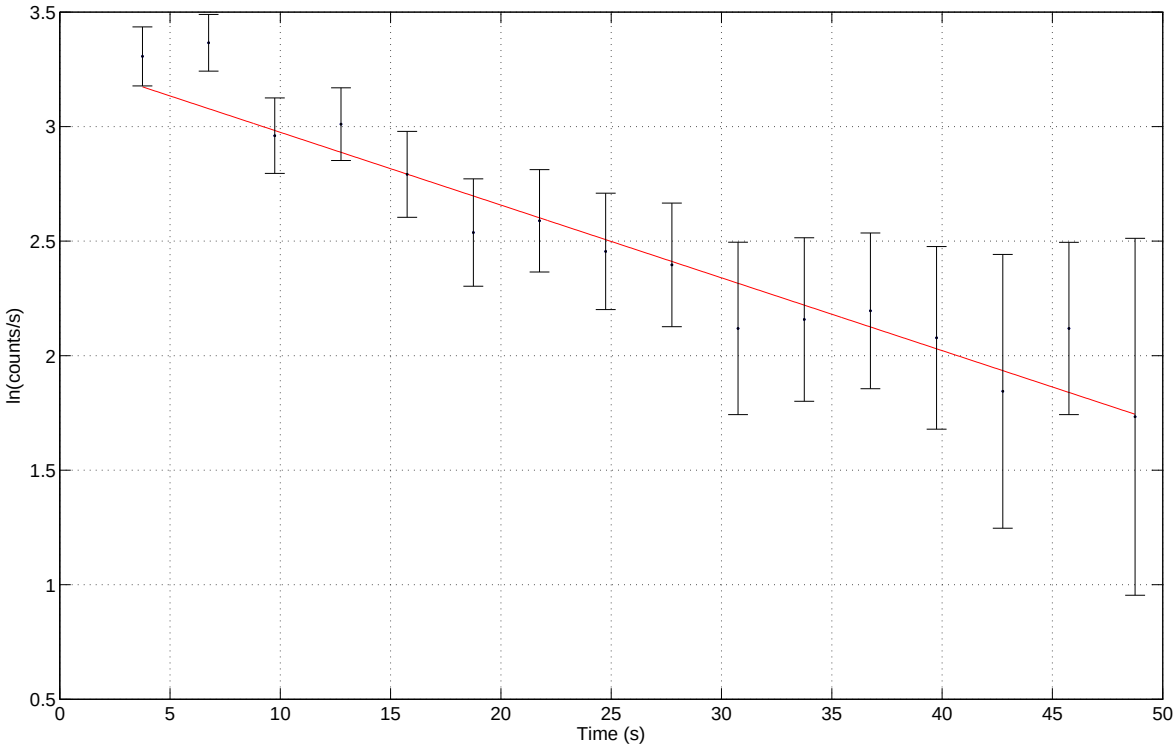

Figure 18: Pd-107 Experimental Half-Life Least Squares Fit

Figure 18 illustrates the difficulty in obtaining a precise half-life due to the increasing size of the error bars as the count rate drops exponentially as time elapses with the initial count rate being approximately 1 count per second from Table 7. The magnitude of the error bars for Figures 18 and 17 is derived from Equation 25.

Figure 19 shows the spectra of palladium-107 and palladium-109 as if the sample was irradiated by the one-shot method described in the literature and the detector was never turned off. The power of the transport system is shown here because the transport time can be determined and all irradiation runs can be compressed into one spectrum to clearly identify the primary gamma peaks of the isotope of interest. Using the HPGe allowed for the clear determination of both isotopes present within the sample when the background had been subtracted. Even though both peaks would show using a sodium-iodide, there would be an overlap between the two gamma rays due to the significant decrease in resolution.

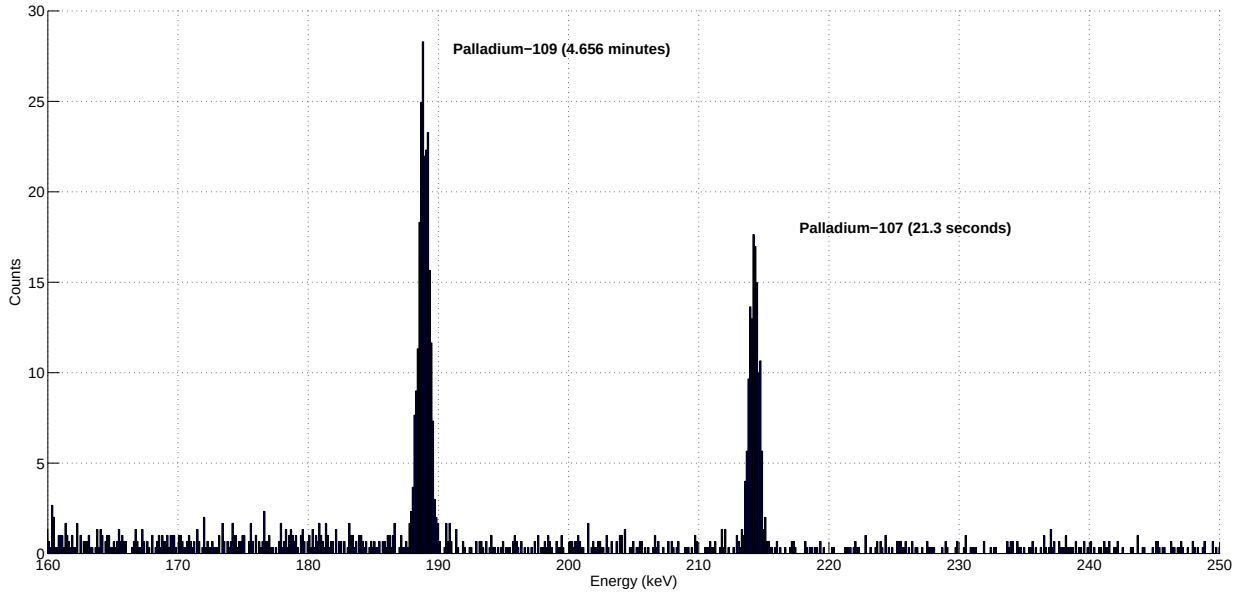

Figure 19: Palladium-107 and Palladium-109 Spectrum

Germanium was chosen in an effort to isolate the signature of germanium-75. This isotope has a longer half-life, but has a significantly smaller resonance capture cross section than the previous two isotopes experimented on shown in Table 6. This experiment will test whether or not the lower limit of the absorption cross section of an isotope has been reached with the system.

Similarly to palladium-107 and palladium-109, germanium-75 is an isotope that has a short-lived internal conversion process that releases a gamma ray. Yet, germanium-75 has the smallest resonance integral and relatively low gamma ray intensity compared to the other isotopes in this thesis. This complicates the situation, since activation in the palladium target had been low already.

Nonetheless, the activation of germanium-75, shown in Table 7, was significant enough to detect with similar difficulty to palladium-107 even with almost a factor of eight reduction in target mass. The reasoning behind this was germanium-74 had a much larger capture probability to the excited state than both palladium isotopes. The two isotopes of palladium and indium studied in these experiments primarily prefer neutron capture to the ground state in the resonance region; which, subsequently prefer β^- decay over internal conversion. The isotope of germanium prefers its excited state, especially in resonance neutron capture, and ultimately goes through the internal

conversion process, shown below. Figure 21 show the spectra of germanium-75 as if the target was irradiated using the one-shot method and the detector was continuously on.

Figure 20 shows the experimental half-life of germanium-75 using a linear least squares fit; and, the difficulty in measuring the half-life precisely due to the wide fluctuations in the count rate after one half-life.

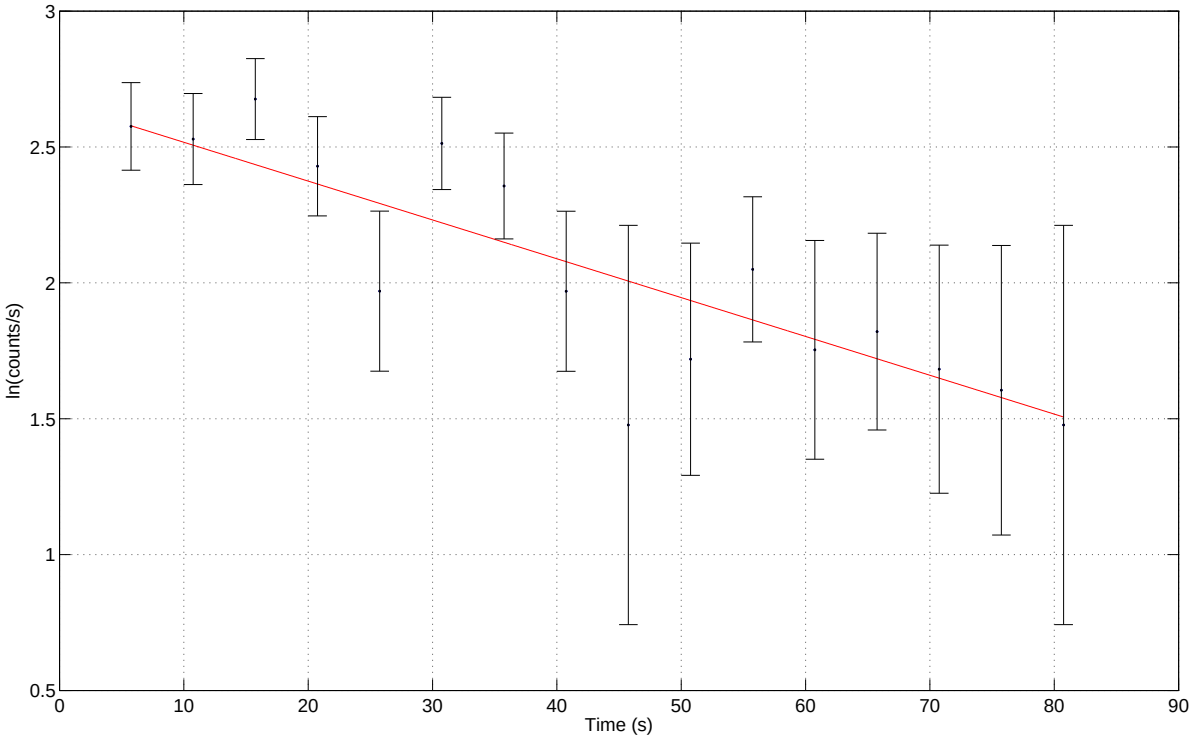

Figure 20: Germanium-75 Experimental Half-Life Least Squares Fit

After eighteen irradiation runs on the germanium target it was possible to measure a half-life that is comparable to the quoted half-life of germanium-75. Unlike the previous experiments with palladium, it was only possible to measure the half-life to a little better than twenty percent error. Due to the reduction in mass of the sample vial, the transport time changed as well. According to Sterlinski, the half-life calculated contains some experimental bias in the result [8].

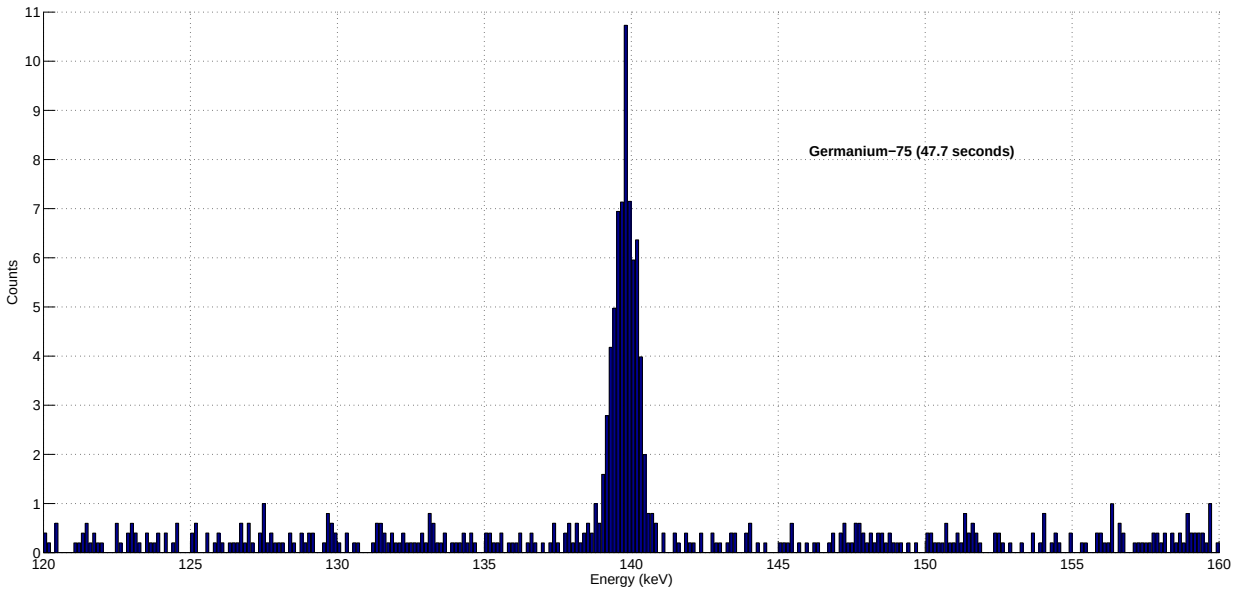

Figure 21: Germanium-75 Spectrum

This issue did not arise with either palladium isotope, but this result was expected due to the cross section for germanium in the resonance region being an order of magnitude less than palladium-107 and two orders of magnitude less than palladium-109; but, a gain in the ease of detection was predicted due to the relatively longer half-life over palladium-107.

Beyond calculating the half-lives of each isotope, as a means of verifying the usefulness of the system the specific activation was calculated for the nuclides that were produced to determine the production of short-lived nuclides that were created per unit target mass. Table 8 shows the specific activation in the units of nano-curies per gram (activation per unit target mass) normalized to the same source strength and the mass of the target material for each isotope.

It was hypothesized that the activation of the target materials would be very low by the neutron generator due to the relatively low source strength, shown in Table 8, but it was not expected that germanium would have the highest specific activation among the nuclides, aside from indium.

Presented in the next chapter, a MCNP model was produced as a means of benchmarking the experimental results, and to determine whether the specific activations and count rates on the

Table 8: Experimental Specific Activation for Various Isotopes of Interest Normalized to Same Source Strength

Isotope	**Target Mass (g)**	**Specific Activation** (nCi/g)
Palladium-109	7.81	158.9
Palladium-107	7.81	49.4
Germanium-75	0.526	504.8
Indium-116	0.344	518.6

detector system were reasonable. This includes modifying the simulated results using the difference between the isotopes neutron captures to the excited state over the ground state. It is postulated that most neutrons are being captured by the target materials in the resonance region.

CHAPTER 5: ANALYSIS OF EXPERIMENTAL RESULTS USING MCNP

The goal of constructing the pneumatic transport system is to estimate the quantities of activation products produced by the neutron generator in indium, palladium, and germanium by neutron activation analysis. Using MCNPX 2.6.0, a spatially accurate model geometry of the graphite pile was created to benchmark the experimental results against simulations.

In the MCNP model, a few assumptions were required, especially with regard to the geometry of the neutron generator. The neutron generator is modeled in MCNP as an isotropic surface source of width 1.118 cm and offset from the end cap by 12.56 cm. However, the neutron generator is an isotropic volumetric source with a slight forward bias due to momentum of the deuteron. Using Equation 28, taken from the ThermoFisher DNCII user guide, the source strength can be determined by the input current and voltage into the DNCII control program where the current is in μA, the voltage is in kV, and the source strength is in neutrons per second,

$$S = 2382 \times I \times V^{\frac{3}{2}}. \tag{28}$$

Using a current of 30 μA and 90 kV in Equation 28, the assumption is the neutron generator will produce approximately 6×10^7 neutrons per second. This information is used as a multiplier to all results produced in MCNP for the simulated comparison presented in this chapter. Figure 23 shows the output of the volume-averaged neutron flux (F4) tally from MCNP where the volume of interest is bounded by the Lexan vial in Figure 22. Directly surrounding the target material is the Lexan sample vial. Surrounding the Lexan sample vial in Figure 22 shows the stainless-steel pneumatic transport tube, where the gas inlet tubing was not included in this model. Surrounding the pneumatic transport tube and the void for the neutron generator encompass the boundary of the volume that is the graphite pile.

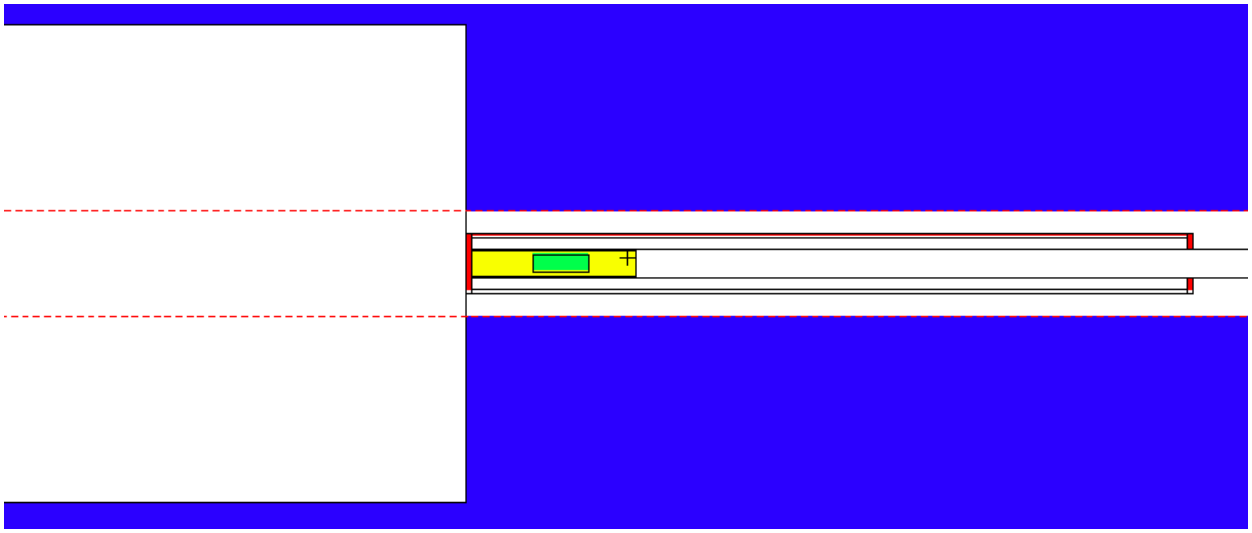

Figure 22: MCNP Geometry of Void Region Encompassing Transport Tube and Neutron Generator

In Figure 23, as expected there is a sharp peak at the source energy (14.1 MeV), a continuous slowing down region, and because of the graphite moderator, a broad peak at thermal energies. Table 9 describes the ratios of capture to the excited state for thermal neutron capture and resonance capture.

Shown in Table 9, each isotope of interest, besides germanium, decay to their the excited state more often from thermal over resonance neutron capture. Germanium instead preferentially chooses the excited state more often upon resonance capture of a neutron. Equation 29 describes the method used to convert the neutron capture tallies produced in MCNP to the expected count rate from the detector,

$$CR = R \times \phi \times V \times \left(\frac{C_i}{C_t}\right) \times \varepsilon(E) \times BR \times BF, \tag{29}$$

where ϕ is the neutron source strength in neutrons/s, V is the volume in cm^3, C_i is the contribution to the reaction rate tally from the isotope of interest, C_t is the contribution to the reaction rate tally from all isotopes in the target material, R is the volume averaged reaction rate tally from MCNP with units $1/cm^3$, $\varepsilon(E)$ is the detector efficiency at the energy of the gamma ray of interest,

BR is the branching ratio of the gamma ray of interest, BF is the branching fraction to the decay mode of interest, and CR is the count rate expected from the detector setup in counts per second (cps). Simulations in MCNP were produced to compare to the experimental results produced in the previous chapter. MCNP was used to simulate the expected reaction rate for each isotope labeled in Table 9 to compare the experimental results.

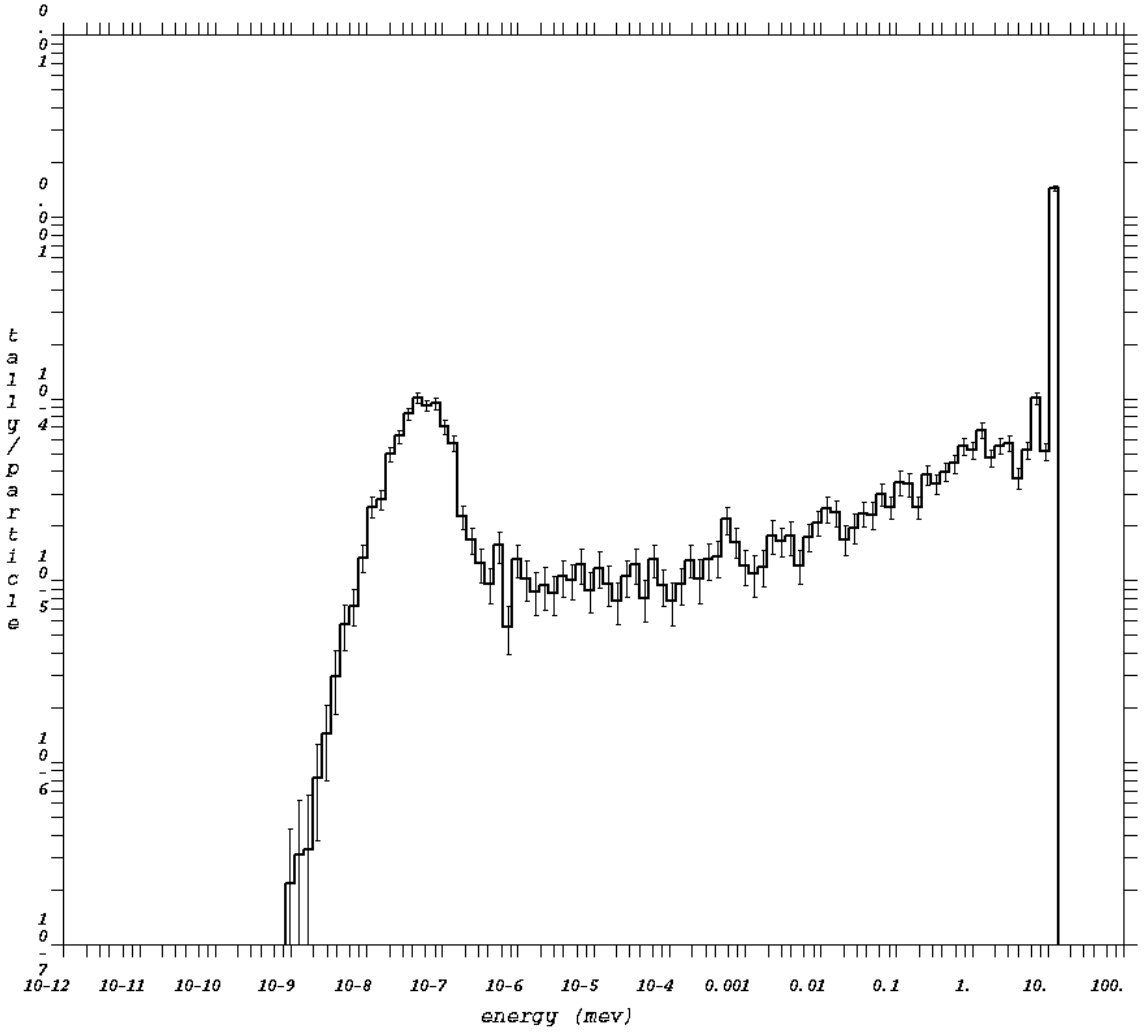

Figure 23: MCNP Neutron Flux (F4) per Source Particle versus Energy in the Target Material

Using MCNP, only neutrons will be counted and the the gamma ray production rate will be calculated from the neutron flux tally multiplied by the neutron capture cross section. With this in mind, it is important to understand the distinction between neutron capture to an excited state versus the ground state and how that affects gamma emission. From Table 9, the experiments rely on resonance absorption as the primary mode of neutron capture; however, the ratio of neutron

captures that lead to the excited state over the ground state must also be taken into account.

For all isotopes listed only captures that lead to an excited state will undergo internal conversion and lead to x-ray and gamma radiation. Thus, Equation 29 does not accurately describe the situation and requires modification to weigh captures to an excited state over captures that lead to the ground state.

Table 9 is taken from the Chart of the Nuclides and describes the ratio of when a thermal neutron interacts with the target nucleus, how often the daughter decays to an excited state over the ground state. Additionally, how often the target nucleus decays to an excited state when a neutron interacts with initial an energy in the resonance region of the neutron absorption cross section of the target nucleus. [2].

Table 9: Cross Section Ratios of Neutron Capture to Excited State versus Ground State [2]

Isotope (Reaction)	**Thermal to Excited State**	**Resonance to Excited State**
Palladium-106 (n,g)	0.013/0.28	0.2/5.5
Palladium-108 (n,g)	0.19/8	2/240
Germanium-74 (n,g)	0.14/0.3	0.4/0.2
Indium-116 (n,g)	41/(75+87)	670/2600

For the isotopes listed above, β^- decay is also a possibility, but does not lead to the half-lives listed in Table 1 and are not short-lived. The fraction of captures to an excited state are only a fraction of captures to ground and reduces the expected reaction rates for every isotope both through thermal and resonant neutron capture. This problem first arose when comparing the reaction rate between experiment and simulation for the indium. Even though the neutron generator was producing significant quantities of activation in the indium target, there was not consistency between experimental results and the simulated results in MCNP.

It was expected that the activation of palladium would be far more significant; however, as Table 10 displays that the palladium target was only able to reach 1/40 of the initial expectation given the results from the MCNP simulations. This weighting factor resulted in better agreement between experiment and simulation. This result is not significant and is accurate to an order of

magnitude, though there was an expectation of a much more accurate simulated result to compare with the experimental results.

Equation 30 shows the correction to yield the modified count rate expected at the detector,

$$CR' = CR \times \left[\frac{NC_{Excited-TH}}{NC_{Ground-TH}} \left(\frac{NC_{TH}}{NC_{TOT}} \right) + \frac{NC_{Excited-EPI}}{NC_{Ground-EPI}} \left(\frac{NC_{EPI}}{NC_{TOT}} \right) \right], \tag{30}$$

where CR is expected count rate computed from Equation 29, $NC_{Excited\text{-}TH}$ is the thermal neutron captures leading to the excited state, $NC_{Ground\text{-}TH}$ is the thermal neutron captures leading to the ground state, $NC_{Excited\text{-}EPI}$ is the epithermal neutron captures leading to the excited state, $NC_{Ground\text{-}EPI}$ is the epithermal neutron captures leading to the ground state, NC_{TH} is the fraction of thermal neutron captures, NC_{EPI} is the fraction of epithermal neutron captures, NC_{TOT} is the total neutron captures, and CR' is the modified count rate.

The comparison between experimental results and simulation for germanium, when comparing the reaction rates to MCNP and using Equation 30, yielded almost a perfect match to the initial concentration that had been achieved experimentally shown in Table 10.

Table 10: Experimental Quantities Versus Simulated Results

Property	**Pd-107**	**Pd-109**	**Ge-75**	**In-116**
Experimental Integrated Count Rate (cps)	0.98	1.00	0.58	13.85
Experimental Activity (Bq)	47.55	51.02	36.84	5442.1
MCNP Reaction Rate (cps) [Equation 29]	4.95	40.91	0.51	51.33
Modified Reaction Rate (cps) [Equation 30]	0.268	1.173	0.58	15.78
MCNP Simulated Activity (Bq)	13.00	59.85	36.84	6200.5
Difference Between Simulation (Equation 30) and Experiment	72.7%	17.3%	0%	12.2%

This is not the case for both palladium isotopes as these results were, at worst, off by approximately a factor of two. The discrepancies between simulated and measured activities are because of the unknown energy that divides thermal and resonance capture from the Chart of the Nuclides [2]. The energy boundary between thermal and epithermal was 100 meV for indium-116, palladium-

107, and palladium-109 in Table 10. However, for germanium the energy boundary was changed to 1 eV for good agreement between the MCNP simulation and the experimental results. After testing this problem extensively in MCNP, it is clear that MCNP does not take capture to an excited state into account and could be amended in future versions of MCNP. For the isotopes listed in this chapter, MCNP only has the cross section data for decay modes to ground states. When MCNP outputs the photon energy versus intensity, it does not include the decay modes for the excited states.

CHAPTER 6: CONCLUSION

In this thesis, the construction of a pneumatic transport system for the explicit purpose of irradiating various target materials using a ThermoFisher P385 D-T neutron generator was described to measure short-lived neutron activation products. The objective of this thesis was to show that a reactor or high-flux neutron environment was not necessary to detect short-lived activation products and that it was indeed possible to successfully measure short-lived neutron activation products with a pneumatic transport system. The sample materials that were irradiated were indium, palladium, and germanium. The longer lived isotopes of indium and palladium-109 and the shorter lived isotopes of palladium-107 and germanium-75 were the activation products that were studied. Even using the neutron generator with its relatively low source strength, it was still possible to successfully measure the half-life of all isotopes that is similar to the quoted half-lives in the reference materials. Surprisingly, it was possible to significantly activate germanium, even though the expectation was palladium-109 and indium would have the highest specific activation, shown in Table 7 from Chapter 4.

Using MCNP, a model was created for each of the experiments to compare the count rates that were expected from the gamma detector. Using the Chart of the Nuclides and ENDF, a modification was introduced to incorporate the ratios of isomeric (excited states) to the ground state reactions from the resulting neutron capture. After applying this modification to the results from MCNP, the conclusion was MCNP was not taking captures to the excited state into account. Instead of simulating a neutron and photon problem, a neutron only problem was simulated and the resulting reaction rates were then modified accordingly. After applying this modification, the results for palladium-107 were still inconsistent between experiment and simulation, shown in Table 10.

The limiting factors after significant experimentation with the target materials described in the previous chapters were the relatively low neutron flux on the target, the low efficiency of the high-purity germanium detector, and the use of thick stainless steel end-caps. However, the benefit

of the HPGe was the significant increase in energy resolution over a sodium-iodide scintillation detector, which allowed for a higher signal to noise ratio. The signal to noise ratio is a key factor in the determination of short-lived neutron activation products because of the low activities generated with the neutron generator from the target materials used. If a x-ray window were installed into the stainless steel transport tube to allow the transmission of x-rays from the irradiated target to the detector, the benefits would be significant during experimentation. This is due to the primary decay mode of short-lived activation products being the internal conversion process. This fact limited the choice of target materials to irradiate, since the materials used in this thesis not only emitted x-rays, but also higher energy gamma rays where the only photons that could ultimately be detected were the only the gamma rays.

CHAPTER 7: FUTURE WORK

There are many improvements that could be made to the pneumatic transport system in the future that were unable to be accomplished in during the research presented in this thesis. The intentions of this thesis were to build, design, and test a pneumatic transport system and show that it was possible to detect short-lived radioisotopes. The pneumatic transport system itself works quite well and can transfer samples in both directions efficiently and consistently; however, an area that needs vast improvement is the entire detector side of the system. Not only is it not feasible to detect x-rays, but because of the low efficiency of high-purity germanium, the detector cannot efficiently detect gamma rays either. To improve on this aspect, a move from high-purity germanium to sodium-iodide would improve the efficiency. Alternatively, since another high-purity germanium is available, the next logical step in improving the system could be to incorporate another high-purity germanium into the setup to increase the total geometric efficiency. Since so many short-lived nuclides rely on internal conversion, the replacement of the end-cap on the detector side with a plastic or aluminum one could be beneficial in allowing more x-rays through to the detector. For samples that decay by β^- emission, it could also be useful to incorporate a beta counting system on top of the gamma spectroscopy system to improve upon the statistical uncertainties that were recognized with palladium-107 and if shorter lived isotopes were chosen.

It seems that using a deuterium-tritium neutron generator might be useful for neutron activation analysis; especially, in areas where one would want portability. However, if portability is not a concern, then a small research reactor provides the ability to interrogate any target material. Even nuclides with very small cross sections could still be easily detected in a reactor environment where the equivalent result from the neutron generator would not yield promising results. The isotope with the smallest cross section of approximately a barn in the resonance region was easily detectable with the neutron generator, but there are many interesting targets with short-lived daughters that the pneumatic transport system could not isolate whose cross sections are in the tenths or hundredths

of barns. This is exacerbated by not being allowed to run the neutron generator at full power. On that note, the results that were achieved in this thesis, in the time that they were achieved, is very promising; but, it is understood that the configuration that had been constructed for this thesis has many limitations.

BIBLIOGRAPHY

[1] Michael D. Glascock. Overview of neutron activation analysis, 2015.

[2] Edward M. Baum. *Nuclides and Isotopes: Chart of the Nuclides*. KAPL, 2010.

[3] Hans-Jurg Kreiner. A high speed conveyer tube system for short-lived nuclide measurements. *Nuclear Instruments and Methods*, 141:119, 1977.

[4] Alfred O. Paas and Robert D. Sullivan. Measurement of neutron activated short-lived nuclides using a pneumatic transfer system. Master's thesis, United States Naval Postgraduate School, 1962.

[5] S. S. Ismail. A new automated sample transfer system for instrumental neutron activation analysis. *Journal of Automated Methods and Management in Chemistry*, 2010, 2010.

[6] I. Salma and E. Zemplen-Papp. Activation analysis with neutron generators using short-lived radionuclides. *Nuclear Instruments and Methods in Physics Research*, B79:564–567, 1993.

[7] N. M. Spyrou. Cyclic activation analysis - a review. *Journal of Radioanalytical and Nuclear Chemistry*, 61.1:211, 1980.

[8] S Sterlinski. The limit of identification for short lived radioisotopes in activation analysis. *Nuclear Instruments and Methods*, 141:329, 1967.

[9] James J. Duderstadt and Louis J. Hamilton. *Nuclear Reactor Analysis*. John Wiley and Sons, 1976.

[10] Glenn F. Knoll. *Radiation Detection and Measurement*, pages 55, 85–94, 120–121, 458. Wiley, 4 edition, 2010.